Growth of three-dimensional fractures, arrays, and networks in brittle rocks under tension and compression

Robin N. Thomas[a,*], Adriana Paluszny[a], Robert W. Zimmerman[a]

[a]*Department of Earth Science and Engineering, Imperial College London*

Abstract

Concurrent growth of multiple fractures in brittle rock is a complex process due to mechanical interaction effects. Fractures can amplify or shield stress on other fracture tips, and stress field perturbations change continuously during fracture growth. A three-dimensional, finite-element based, quasi-static growth algorithm is validated for mixed mode fracture growth in linear elastic media, and is used to investigate concurrent fracture growth in arrays and networks. Growth is governed by fracture tip stress intensity factors, which quantify the energy contributing to fracture extension, and are validated against analytical solutions for fractures under compression and tension, demonstrating that growth is accurate even in coarsely meshed domains. Isolated fracture geometries are compared to wing cracks grown in experiments on brittle media. A novel formulation of a Paris-type extension criterion is introduced to handle concurrent fracture growth. Fracture and volume-based growth rate exponents are shown to modify fracture interaction patterns. A geomechanical discrete fracture network is generated and examined during its growth, whose properties are the direct result of the imposed anisotropic stress field and mutual fracture interaction. Two-dimensional cut-plane views of the network demonstrate how fractures would appear in outcrops, and show the variability in fracture traces arising during interaction and growth.

Keywords: fracture growth, fracture interaction, fracture networks, fracture

*Corresponding author

Email address: robin.thomas10@imperial.ac.uk (Robin N. Thomas)

mechanics, stress intensity factor, quasi-static growth

Key Points

- A fracture mechanics based numerical method for growing multiple three-dimensional fractures in mixed mode conditions is introduced
- Fractures develop complex non-planar surfaces as a result of interaction in arrays and networks
- Cut-plane visualisation of three-dimensional fractures surfaces enables direct comparison to outcrops and experiments

1. Introduction

Constraining the properties of fractured rocks is of great interest in subsurface science, particularly for applications such as radioactive waste disposal [1], reservoir engineering [2], CO_2 storage [3], and geothermal energy production [4]. Understanding and modelling of fracture growth is an important method for characterising rock. Fractures which have grown due to mechanically induced stresses are prevalent in the subsurface. The presence of a fracture changes the concentration of stress in a rock, and this change varies based on the fracture's geometry and the local stress tensor [5].

Fracture arrays in rock outcrops demonstrate the complexity arising when fractures mutually interact. Fracture hooking reflects the balance between far-field stresses and fracture interaction forces [6–8]. Curved paths suggest that remote stresses are nearly isotropic relative to the stresses induced by fractures. Furthermore, the onset of fracture connectivity has significant implications for the hydraulic properties of rock [9]. Fracture mechanics seeks to describe the physical processes taking place at each step of fracture extension, but analytical

approaches are limited to specific geometries [10]. Experimental approaches provide a basis for the current understanding of the fracture propagation in rocks, including characterizing three-dimensional internal fracture geometries for a variety of natural and engineered materials [11].

Modelling the growth of a medium containing multiple fractures, including non-planar fracture surface accretion and interaction between fractures, requires an advanced approach which incorporates the physics of linear elastic fracture mechanics. Numerical methods seek to overcome scale and geometric limitations by modelling the physical processes that control deformation. The geometry of fractures can be explicitly modelled to track changes in fracture shape during growth, capturing the effects of propagation in response to mechanical forces. The discrete representation of a fracture, where both the matrix domain and fracture domains are discretised, is instrumental when solving flow and transport equations in fractured media [12, 13].

A variety of approaches are used to model the growth of 3D discrete fractures, including the finite element method (FEM) [14, 15], extended finite element method (XFEM) [16–18], boundary element method (BEM) [19, 20], displacement discontinuity method (DDM) [21, 22], phase field method [23], and the discrete element method (DEM) [24–27]. Hybrid methods incorporate multiple methods to handle different parts of the implementation, such as solving for stress and displacement in the solid using the FEM, and managing geometry using the DEM [28–30]. When modelling discrete fractures, methods where fracture paths are restricted by pre-existing discretisation are unsuited to predicting of fracture growth. DEMs require micro- to macro-calibration of material properties that are rock type and scale dependent. The phase field method often requires very refined meshes in order to represent high aspect ratio fractures. XFEMs avoid re-meshing by representing fractures as a shape

function discontinuity, but often require re-meshing in order to resolve stresses and fracture propagation in initially coarsely discretised regions of the model [31, 32].

The growth of multiple discrete fractures in response to deformation and flow results in a combination of complex geometric fracture shapes that reflect both the physical processes of deformation and the underlying structure of the material [33]. Discrete fracture growth approaches which utilise linear elastic fracture mechanics theory calculate either the stress or the stress intensity factor (SIF) at fracture tips to handle growth. Methods for modelling non-linear growth during more complex constitutive behaviour such as thermo-poroelastic [34] and visco-elastic [35] deformation have also been developed. SIF based approaches have been used to grow 2D fractures in populations [36], often with interest in the ensuing changes on the hydraulic properties of the domain [37, 38].

The availability of mixed mode failure criteria provides the possibility of growing fractures under conditions where fracture surface contact significantly alters the tip conditions [39]. Numerical modeling extends this concept to larger populations of fractures, providing a methodology to generate geomechanically realistic discrete fracture networks, in which connectivity is a function of density increase and topology changes driven by growth. The relative propagation rate between locations along the edge of one fracture, or, over different fractures in a population, exerts a fundamental control on final geometries [6]. Low velocity growth produces patterns where many fractures are active, where fractures grow below the critical toughness of the material in small increments, and high velocities produce the opposite, where growth is restricted to only a few fractures. A fracture mechanics-based approach can consider these cases as a continuum by using a Paris-type law which, depending on the fracture growth exponent, can be used to govern the extension of slow and fast fractures [40].

Fracture growth methodologies which advance fractures in discrete steps, referred to in this work as "quasi-static growth schemes" [*e.g.* 19, 41–45], will have similar properties due to the requirement to advance fracture tips in discrete steps. Quasi-static growth is a reasonable assumption for subsurface fracture networks, where growth occurs locally in short ruptures, and by chemically assisted processes such as stress corrosion [46], tectonic stresses [6] and thermal deformation. A quasi-static approach also enables the stress driving fracture growth to be re-sampled regularly, allowing fracture geometries to be continuously updated. This ensures the correct growth direction is maintained throughout the modelling workflow.

This work outlines a finite element-based approach to numerically model three-dimensional discrete fracture growth under mixed mode conditions in brittle material. This quasi-static growth methodology is developed within the Imperial College Geomechanics Toolkit (ICGT) [47, 48]. This work validates fracture growth, examines the implications of using a quasi-static growth method, and in the process, demonstrates that realistic geometries arise as a result of the adopted fracture mechanics-based approach. In Section 3, the accuracy of the stress intensity factor computation is quantified in terms of the mesh refinement, and recommendations are made for selecting appropriate parameters for sampling mechanical variables around fracture tips. The growth of individual fractures is validated for tension and compression in Section 4. Section 5 explores the growth of fracture arrays, examining in detail different fracture growth rate exponents, including a critical analysis of quasi-static growth phenomena. Section 6 demonstrates the generation of a dense geomechanical fracture network and the realistic features which emerge in the network as a result of the physics-based growth method.

2. Methodology

The present method handles fracture growth quasi-statically, discretely representing fractures as surfaces which extend based on rigorous fracture mechanics principles. Solid deformation and fracture surface contact are resolved using the finite element method, on meshes generated to conform to the changing fracture geometry in each step. The method combines stress intensity factor computation and gap-based Augmented-Lagrangian contact modelling in order to predict and govern the growth of fractures [5, 49, 50]. These advancements enable accurate, concurrent growth of multiple discrete fractures under mixed mode conditions.

2.1. Fracture geometry and discretisation

The geometry of the domain is tracked independently of the underlying discretising mesh [48]. Thus, fracture propagation is determined by the local stress and displacement in the material around the fracture tip, rather than pre-defined path between elements. Fractures grow in response to deformation, and guide the evolving discretisation requirements of the domain, which is automatically generated for each step using a commercial octree meshing platform [51]. The surface of the fracture is discretised using isoparametric quadratic triangles. Figure 1A shows the mesh created for a simple penny-shaped fracture. The finite elements shown are 2D isoparametric quadratic triangles, representing the planar surface of the circular fracture.

Each fracture has two identical sets of surface elements which are coincident (*i.e.*, have no initial aperture) and only connect at the tips, as shown in Figure 1B. The split mesh causes fractures to be treated as a void in the material during deformation. Quarter point elements are used along fracture tips to improve the accuracy of SIF computation (see Section 2.4.1). One individual "fracture tip" is defined as the edge of a triangle shared by two surface elements

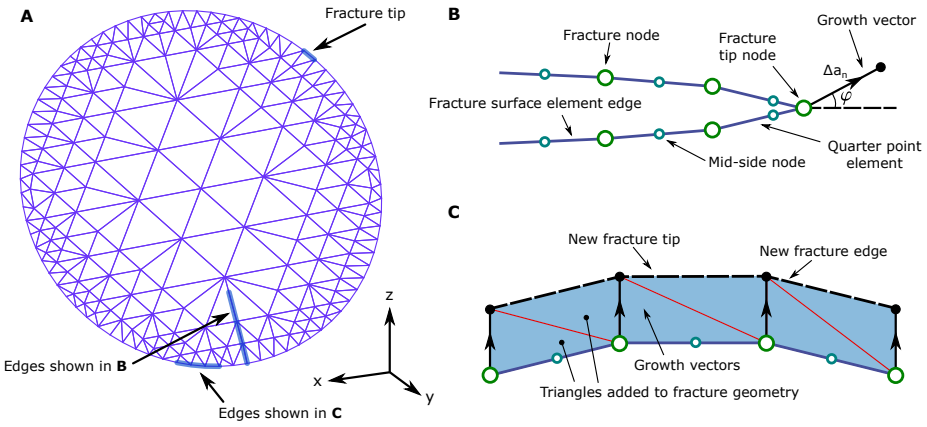


Figure 1: A: Penny-shaped fracture discretised using isoparametric quadratic triangles. B: Schematic of highlighted element edges in A, demonstrating the two coincident fracture surfaces. The fracture deflection angle φ is shown with a growth vector from the tip. C: Schematic of the addition of new fracture surfaces. Growth vectors provide new tips at their ends and a new edge by connecting these tips. The area between the old and new tips is filled with two triangles.

connecting where the fracture terminates. Therefore, a "tip node" is a node on one of these edges, and the "tip loop" comprises all of the fracture tips of one fracture.

The volumetric domain representing the material is discretised using isoparametric quadratic tetrahedra. In order to automate discretisation, the density of finite elements is controlled by the length of the local fracture tips (B_d) [5]. The minimum length of the side of the triangular elements along a fracture's tip is controlled by the distance between tip nodes. In turn, this sets the size of the surrounding surface and volumetric elements, which increase in size gradually further away from the fracture. After fractures in the domain are extended, before the next growth step, the domain discretisation is updated, such that the new mesh conforms to the geometry of the extended fracture.

Figure 2 shows four examples of fractures at different tip node numbers, and the meshes which are generated around them. For a domain containing one fracture, there is a linear correlation between the number of tip nodes around

the fracture (N_f) and the number of elements in the mesh.

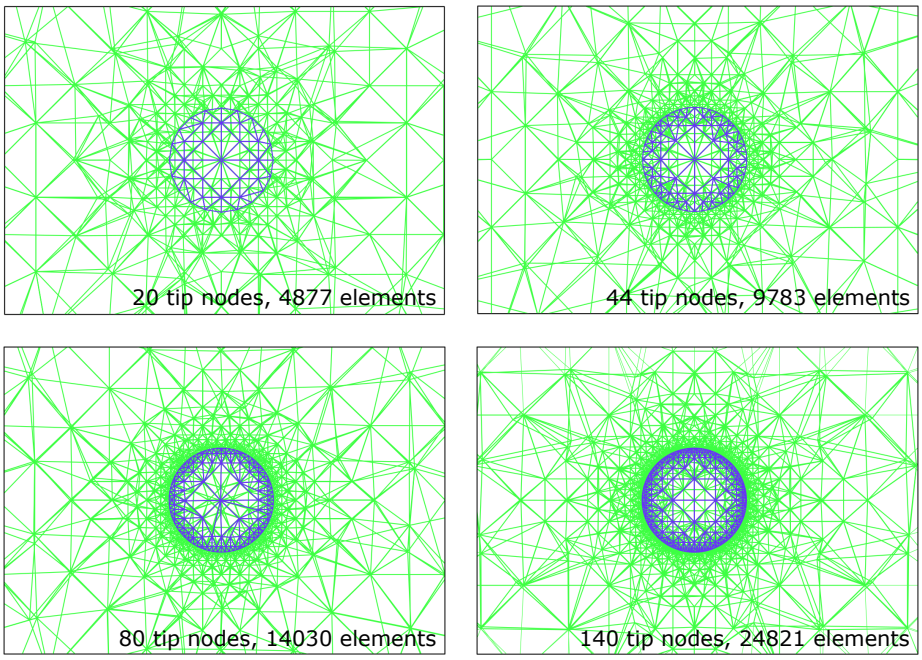


Figure 2: Mesh densities of four example fractures with different numbers of tip nodes. Triangular fracture surface elements are shown in blue, and volumetric tetrahedral elements are shown in green. The number of elements is for the entire volume. A cut is taken through the volumetric mesh to visualize the mesh around the fracture, meaning some volumetric elements appear elongated.

2.2. Deformation

The method has two available methods for computing stress and deformation in the domain in response to a boundary stresses or displacements. The first of these uses the linear elastic deformation method of Cook et al. [52], which is also used in previous versions of this growth methodology [5, 47, 48], and is suited to deforming domains in tension. Section 2.3 describes the contact method used when the domain is under compression or shear.

The rock matrix is assumed to be linear-elastic, homogeneous, and isotropic.

Stress and strain are governed by

$$\sigma = \mathbf{D}(\varepsilon - \varepsilon_0) + \sigma_0 \tag{1}$$

where σ is the Cauchy stress tensor, ε is the infinitesimal strain tensor, σ_0 and ε_0 are the initial stress and strain, and $\mathbf{D}$ is the linear elastic stiffness matrix [52]. The force balance of the system is governed by

$$\underline{\partial}\sigma + F = 0 \tag{2}$$

where $\underline{\partial}$ is the differential matrix operator, and F represents body forces exerted on the object. The system is solved numerically using the finite element method (FEM), over an automatically generated mesh created from the domain's geometry (Section 2.2). For models where fracture surfaces are not expected to be in contact, a single FEM inversion is required to calculate the stress and deformation.

2.3. Fracture surface contact

Friction between the two surfaces of a fracture can have a significant effect on the stress state at its tips [53]. Contact between fracture surfaces can occur under most stress conditions, and is particularly important to consider during compression or shear. The gap-based Augmented-Lagrangian contact resolution method, proposed and validated by Nejati et al. [50], resolves the effect of friction on fracture growth. This enables accurate calculations of stress near the fracture tips for boundary conditions which would lead to fracture surface contact.

The gap-based Augmented-Lagrangian method is a double loop algorithm, using the Newton-Raphson method in the inner loop to solve the contact problem itself, and the augmentation process as the outer loop. A strict penalty parameter, defined as a varying function of the aperture across the fracture sur-

face, ensures that fracture surfaces do not intersect. Even slight intersections are strictly penalised due to a singularity in the penalty parameter at the fracture tips. The result is a fully resolved traction and aperture distribution across the surface of each fracture. These tractions are taken into account in the computation of local SIFs. Nejati [54] details the gap-based Augmented-Lagrangian method in full, and the present work demonstrates how it can be used to grow fractures under compression (see Section 4.2).

2.4. Fracture growth methodology

Following the computation of the stress and displacement throughout the domain, fracture tip stress intensity factors are calculated, which govern the growth process (Section 2.4.1). These values are used in three fracture mechanics-based propagation criteria (Sections 2.4.2, 2.4.3, and 2.4.4) to create growth vectors which extend fracture surfaces.

2.4.1. Stress intensity factor computation

Stress intensity factors (SIFs) quantify the energy at the tip of a fracture in three deformation modes: opening (mode I), in-plane shear (mode II) and out-of-plane shear (mode III). If the value of the SIF for each of these modes is known (K_I, K_{II}, and K_{III}), growth criteria can be evaluated to decide whether the fracture grows, and at what length and angle it extends at. The model applies the disk-shaped domain integral method to calculate the SIFs, outlined in full by Nejati et al. [49], which evaluates the interaction (I) integral around the tip of the fracture. Instead of integrating over a structured concentric mesh, the I-integral is solved numerically over a 2D virtual disk, embedded in the 3D matrix. The I-integral computes the value of the strain energy release rate, $\mathcal{G}$, from which separate the values of K_I, K_{II}, and K_{III} are calculated [55].

An alternative SIF calculation method is the Displacement Correlation (DC) method. It samples only two points behind the fracture tip, and determines the

SIFs based on their relative displacement. The DC method has been validated for tetrahedral domains with quarter-point elements at the fracture tip by Nejati et al. [56]. DC has several benefits over the disk-shaped domain integral method, including its fast computation time and smaller sampling region. It has been shown to be less accurate than the disk-shaped domain integral [5], contour integral, or cutoff function methods [57] for a variety of meshes. The present work uses DC to provide a comparison to the disk-shaped domain integral in Section 3, and to grow the geomechanical discrete fracture network examined in Section 6.

For both the disk-shaped domain integral and the DC method, a domain radius (R_d) must be defined, setting the size of the region sampled around the fracture tip. For the disk-shaped domain integral, the domain is the radius of integration around the fracture tip. For DC, the domain radius is the distance at which the displacement field is sampled. The choice R_d has a complex relationship with the accuracy of the SIFs, explored in detail by Nejati et al. [49]. Large values of R_d violate the assumption of plane strain conditions by sampling too far away from the tip, whilst small domains may sample the fracture tip fields in regions where the numerical error is highest. In growth simulations where fracture tip discretisation is dynamic, R_d must therefore depend on fracture tip properties. Nejati et al. [49] quantified R_d using the average fracture tip length $L_n = L_f/N_f$, where L_f is the fracture circumference, and found that the most accurate results were obtained when R_d is in the range of 0.5 - 1.5 L_n, with 0.5 being more appropriate for coarse meshes and 1.5 for fine meshes.

A novel formulation of R_d is proposed and used in this work, where R_d is calculated at each fracture tip at each step based on the size of the local fracture tip,

$$R_d = 0.5\,|B_d| \tag{3}$$

where B_d is the local tip segment length. The factor of B_d depends on local mesh density, and for this work 0.5 is chosen to ensure results are as accurate as possible in coarsely meshed domains [49]. This formulation ensures accurate values of the SIFs are computed when tip segment sizes vary due to fracture propagation, because R_d will always have a value based on the size of local elements, rather than fracture size which changes during growth simulations. Section 3 validates Equation 3 for penny shaped fractures in tension and compression.

2.4.2. Propagation criterion

Fracture propagation is a combined response to all three deformation modes. A mixed mode failure criterion responds to tension and shear simultaneously for loading, including tension, compression and shear [58]. Three-dimensional mixed mode criteria determine if a fracture will propagate based on a comparative stress intensity factor (K_v), derived from the values of K_I, K_{II} and K_{III}, exceeding the local fracture toughness of the material [59]. Richard et al. [58] reviewed a range of criteria and compared their predictions to experimental data, demonstrating that the most accurate condition for fracture failure is

$$K_v = \frac{K_I}{2} + \frac{1}{2}\sqrt{K_I^2 + 4(\alpha_1 K_{II})^2 + 4(\alpha_2 K_{III})^2} = K_{IC} \tag{4}$$

where α_1 and α_2 are the ratios of the mode I fracture toughness to the mode II and III fracture toughness ($\alpha_1 = K_{IC}/K_{IIC}$, $\alpha_2 = K_{IC}/K_{IIIC}$, where subscript C refers to the critical stress intensity factor). For rocks, values of K_{IIC} tend to be higher than K_{IC}, and K_{IIIC} tend to be lower. In this work, $K_{IC} = 1{\times}10^6$ Pa, $K_{IC}/K_{IIC} = 1/1.3268$, and $K_{IC}/K_{IIIC} = 1/0.6297$, as found through studies investigating the point of failure for pure modes II and III in rocks [60–62].

2.4.3. Angle criterion

If the failure criterion is met at a fracture tip, the mixed mode criterion of Richard et al. [59] calculates the angle of the fracture propagation vector as a function of its modal SIFs. It calculates two angles that are perpendicular and tangent to the fracture front, and has been experimentally validated [39]. The perpendicular angle (φ, or fracture deflection angle along its plane) is calculated from the three SIFs as follows:

$$\varphi = \mp \left[A \frac{|K_{II}|}{K_I + |K_{II}| + |K_{III}|} + B \left(\frac{|K_{II}|}{K_I + |K_{II}| + |K_{III}|} \right)^2 \right] \tag{5}$$

where A = 140° and B = -70°. φ is negative when $K_{II} > 0$ and positive for $K_{II} < 0$ and $K_I \geq 0$. K_I is capped at zero to avoid introducing errors into the propagation angle. This can arise if a fracture closes from an initially open state. Figure 1 shows the fracture geometry (A) and tip (B), including a vector with angle φ in the context of a discretised fracture tip.

A second angle, the twisting angle ψ, also modifies the propagation direction tangent to the fracture tip, and is calculated in a similar way to φ:

$$\psi = \mp \left[C \frac{|K_{III}|}{K_I + |K_{II}| + |K_{III}|} + D \left(\frac{|K_{III}|}{K_I + |K_{II}| + |K_{III}|} \right)^2 \right] \tag{6}$$

where C = 78° and D = -33°. The value of ψ is incorporated into validating the present method by testing the accuracy of fracture propagation in Equation 11. It is not incorporated into growing fractures in this work, to avoid additional complexities which arise when fracture tips fragment, such as tip fragmentation [63, 64]. For fractures growing in mixed mode or mostly mode I conditions in the present work, excluding the tangent angle is found to still produce accurate growth. In future work, growth vectors incorporating the tangent angle can be incorporated to model growth driven by twisting (mode III). Amongst a range of

different criteria for estimating the propagation angle of fractures under mixed mode loads, Equation 5 was found to be the most accurate at predicting growth paths which emerge from experiments, with the most deviation for pure mode III and pure mode II and III loading [39]. These less accurate modes of growth are not the focus of the present work, which focuses more on mixed conditions where mode I is the largest, or when all three modes have similar magnitudes.

When K_I is negative due to a closing fracture tip (*e.g.*, in the case of an initial fluid pressure opening the fracture), K_I is set to zero when evaluating the propagation and angle criteria. Thus, in this case, failure is based purely on the shear modes. This is particularly important when calculating Equation 5 where K_I is reckoned positive. This ensures growth can occur in all cases in the present method, and also highlights that propagation during closure is not necessarily predicted by the criteria of Richard et al. [59].

2.4.4. Length criterion

This section describes the method by which the extension length for each tip is calculated, provided those tips meet the failure criterion in the domain (Equation 4). Two-dimensional numerical studies show that within a group of fractures, in order to reproduce patterns found in growth experiments, crack fronts must grow at different speeds [36]. In three-dimensions, each point along the fracture tip may have a different growth extent. Furthermore, the relative extension length at each tip in each step must be influenced by the competitive process of growth during interaction. This section introduces a new criterion to govern the quasi-static propagation of multiple fractures, devised to generate realistic fracture patterns similar to those observed in rock outcrops.

There are two primary energy-based methods used to quantify growth extent in rocks. The first method, sub-critical crack growth theory, is widely used to study growth of fractures through the relationship between the velocity of

tip advance and the magnitude of K_I [65]. The relative growth velocity criterion was first proposed by Charles [66] and was extended to a relative growth extension criterion by Renshaw and Pollard [36]. The theory incorporates the effects of non-mechanical effects, including the rate of stress corrosion reactions at the fracture tips [67]. The second method is the Paris-type criterion governing fatigue fracture growth, and quantifies the advance of a fracture tip per load cycle [68]. This criterion proposes that the extension of a fracture front point is proportional to the point-wise energy release rate, such that the point with the maximum energy release rate grows fastest, while other points grow proportionally slower [69].

Both the Paris and sub-critical crack growth methods both take the form of a power law [67, 69]. In the context of cyclical loading with reversed stresses, this criteria takes the form:

$$\frac{\mathrm{d}a}{\mathrm{d}N} = c\left(\frac{\mathcal{G}}{\mathcal{G}_{max}}\right)^{\beta} \tag{7}$$

where $\mathrm{d}a/\mathrm{d}N$ is the advance of the fracture tip per load cycle N, c is a material constant, $\mathcal{G}$ is the value of $\mathcal{G}$ at the tip in question, $\mathcal{G}_{max}$ is the largest value of $\mathcal{G}$ among present fractures, and β is the fracture growth rate exponent. In a quasi-static growth scheme, each load cycle N is one growth step, which may have timescale.

In the context of sub-critical crack growth, $\mathcal{G}$ is typically exchanged for K_I, as most analyses consider only mode I, and $\mathrm{d}a/\mathrm{d}N$ is exchanged for the growth velocity [70]. The constant c and β have different units in each method, and are estimated through different methods. For a domain containing many fractures which grow quasi-statically at a variable length along their tips, both methods predict that the exponent β controls the extent to which growth is concentrated at tips with higher energy.

Lazarus [40] notes that the Paris law can be applied to both brittle and fatigue propagation. For fatigue fracture growth, $\beta \approx 1$, and, for brittle fracture growth, $\beta >> 1$. Lazarus [40] shows that, for three-dimensional single fracture growth, this exponent defines the relative extension of the tip nodes of a single fracture. However, a wide range of estimates are made for the value of the fracture propagation exponent. Renshaw and Pollard [36] estimated that $\beta = 0.35$, based on outcrop observations and two-dimensional laboratory experiments in brittle rocks. It was later shown that this exponent affects the type of ensuing fracture pattern [6], with higher values increasing the localisation of fracture patterns [12]. For individual fractures propagating in one plane, the final geometry is highly influenced by the value of β, whilst still converging on circular shapes [40, 71]. In sub-critical growth experiments with few fractures, the value of the exponent is found to be much higher, between 30 and 60 [67]. In the present case, where multiple fractures grow together in three dimensions, high values of β reduce the extent to which fractures grow simultaneously, enhancing interaction effects. In outcrops, multiple fractures are seen to have grown together [7], demonstrating that lower values of β are applicable to slow, fatigue-like growth of arrays.

This work introduces a novel formulation based on Equation 7 for handling propagation in domains containing multiple three-dimensional fractures. Rather than defining a single value of β, two values are defined, β_f and β_n. In each step, a maximum extension length per growth step, Δa_v, is selected. Each fracture tip node n will have a unique energy release rate ($\mathcal{G}_n$) value, amongst which specific values are found: $\mathcal{G}_f$, the highest value of $\mathcal{G}_n$ on each fracture f, and $\mathcal{G}_v$, the largest value of $\mathcal{G}_n$ throughout the volume. Each fracture f is assigned a maximum extension length, Δa_f, which is scaled from Δa_v, based on the ratio

between $\mathcal{G}_f$ and $\mathcal{G}_v$:

$$\Delta a_f = \Delta a_v \left(\frac{\mathcal{G}_f}{\mathcal{G}_v} \right)^{\beta_f} \tag{8}$$

where β_f is the fracture growth rate exponent. Second, using the computed Δa_f value, the local tip extension Δa_n for a tip n on fracture f is given by

$$\Delta a_n = \Delta a_f \left(\frac{\mathcal{G}_n}{\mathcal{G}_f} \right)^{\beta_n} \tag{9}$$

where β_n is the tip growth rate exponent. The amount of growth in each step can be controlled through Δa_v, as this sets the maximum growth extent, and in a domain with multiple fractures and varied values of $\mathcal{G}_n$ along their tip nodes, $\Delta a_n \leq \Delta a_f \leq \Delta a_v$.

This approach essentially applies the Paris-type criterion twice: once to define a maximum extension per fracture (Equation 8), and a second time to define the variation in extension along the fracture tip (Equation 9). In a domain with one fracture, the method is equivalent to a standard Paris law (Equation 7), because that fracture will always have $\mathcal{G}_f$ at a node on its tip, and therefore Δa_f will be the same as $\mathcal{G}_v$. Additionally, either step can be skipped by setting its respective value of β to zero, allowing a single step Paris-type law to be tested without changing the approach. In a domain which contains multiple fractures, $\mathcal{G}_n$ varies widely across many tips. It may be the case, particularly due to fracture interaction, that one value of $\mathcal{G}_n$ is much larger than the others. The present formulation ensures that growth can be distributed across multiple fractures whilst still weighted towards tips and fractures which have the highest values of $\mathcal{G}$ in the domain. The present quasi-static method does not have an associated timescale for each growth step, therefore the Paris-type law is used here to predict relative growth extents, rather than growth velocities. With an alternative FEM formulation which incorporates time based effects, this can

be explored in future work. The implications for use of the modified two-step Paris-type are examined in Section 5.

2.5. Fracture extension

At each fracture tip, a growth vector can be defined with length derived from the modified Paris law, and direction by the angle criterion. The extended fracture geometry is updated by creating a new fracture edge along the points at the end of each vector, as shown in Figure 1C. This can be defined as a strip of triangles or as a deformation of the spline representing the fracture surface [48]. The geometry is updated by placing two triangles between each pair of tips. Where growth vectors intersect other fracture surfaces and boundaries, they are truncated. If two vectors intersect adjacent domain boundaries, the corner between those boundaries is filled by a single triangular surface.

The model geometry, with the addition of new fracture surfaces, is brought forward to the next step and subsequently the domain is remeshed (Section 2.2), such that the mesh is most refined around the new tips. If a fracture propagates into another surface element (*i.e.*, the model boundaries or another fracture), the propagation vector is truncated and the fracture tip at that point is deactivated in subsequent steps. An algorithm describing the steps in the model is given in Algorithm 1.

The computational time required to simulate growth depends on the domain's complexity. On a 2.7GHz Intel Xeon CPU (two processors and 24 physical cores), a single fracture in tension (Figure 4, initially meshed with 7600 elements and 9940 nodes) completed 30 growth steps in 20 minutes. A more complex domain containing sixty fractures (Figures 9 and 10, initially meshed with 174,297 elements and 226,835 nodes) completed 33 steps in 19 hours, including time spent outputting calculated variables.

```
Define geometry of initial fractures and matrix
while current growth step number < maximum growth steps do
    Define matrix and initial fracture geometry
    Discretise volume and surfaces
    Assign material properties and apply boundary condition
    Compute deformation (σ and ε, Equation 1)
    Resolve fracture surface contact and friction
     (Augmented-Lagrangian gap based algorithm, Section 2.3)
    Compute mechanical apertures
    for each fracture do
        for each tip node n do
            Compute R_d (Equation 3)
            Determine K_I, K_II, K_III (Section 2.4.1) and K_V
             (Equation 4)
            if K_V ≥ K_IC then
                Compute Δa_n (Equations 8 and 9)
                Compute φ and ψ (Equation 5 and 6)
                Assemble growth vector and compute new tip location
                 (Section 2.5)
            end
        end
        Geometrically resolve intersections against boundaries and other
         fractures
        Update fracture geometry
    end
end
```

Algorithm 1: Finite element based quasi-static fracture growth algorithm.

3. Stress intensity factor and propagation angle accuracy

This section describes the validation of SIFs and propagation angles for a range of mesh refinements and boundary conditions. Previously, the accuracy of SIFs have been assessed for static fractures by Nejati et al. [49] for the disk-shaped domain integral, Nejati et al. [50] for contact, and Thomas et al. [5] for interaction. The errors in the SIFs and the angles of fracture propagation are quantified to validate fracture growth.

SIFs are compared to analytical solutions for tension [72] and compression in slip and stick [54]. The SIF error e_K is be calculated as a single value for

each fracture, combining all three modes:

$$e_K = \frac{\sum_{i=I}^{III} \int_{L_f} \left| K_i^A - K_i^N \right| dl}{\sum_{i=I}^{III} \int_{L_f} \left| K_i^N \right| dl} \tag{10}$$

where i is one of the three deformation modes (I, II, or III), L_f is the fracture circumference, K_i^A is the relevant analytical solution for the mode i SIF, K_i^N is the numerical solution for the mode i SIF, and dl is the distance between fracture tip nodes [5].

To relate e_K directly to fracture growth, the numerical propagation angles φ^N and ψ^N are compared to the analytical propagation angles φ^A and ψ^A obtained from the analytical SIFs. The propagation angle error, e_a is defined as

$$e_a = \frac{\int_{L_f} \left| \varphi^A - \varphi^N \right| dl + \int_{L_f} \left| \psi^A - \psi^N \right| dl}{\int_{L_f} \left| \varphi^A \right| dl + \int_{L_f} \left| \psi^A \right| dl} \tag{11}$$

Therefore, Equation 11 method provides the cumulative error along the entire fracture tip.

Figures 3 compares the number of fracture tip nodes to e_K and e_a for tension, compression in stick, and compression in slip. To produce slip and stick conditions, the friction coefficient is set to 0 and 100 respectively in the compressive cases. Other material properties are Young's Modulus = 10×10^9 Pa, Poisson's ratio = 0.3, $r = 1$ m, and $\sigma = \pm 1 \times 10^7$ Pa. The bottom boundary is fixed, and the remaining boundaries are traction free. In order to have non-zero SIFs in stick conditions (to generate graphs C and F), a fluid pressure of 5×10^6 Pa is applied uniformly across the fracture surface, providing an initial aperture.

The increase in SIF and propagation angle accuracy with mesh refinement is consistent for all boundary conditions. The disk-shaped domain integral with quarter point elements is the most accurate method for almost all mesh refinements, with some exceptions when fewer than 20 tip nodes are used. Quarter

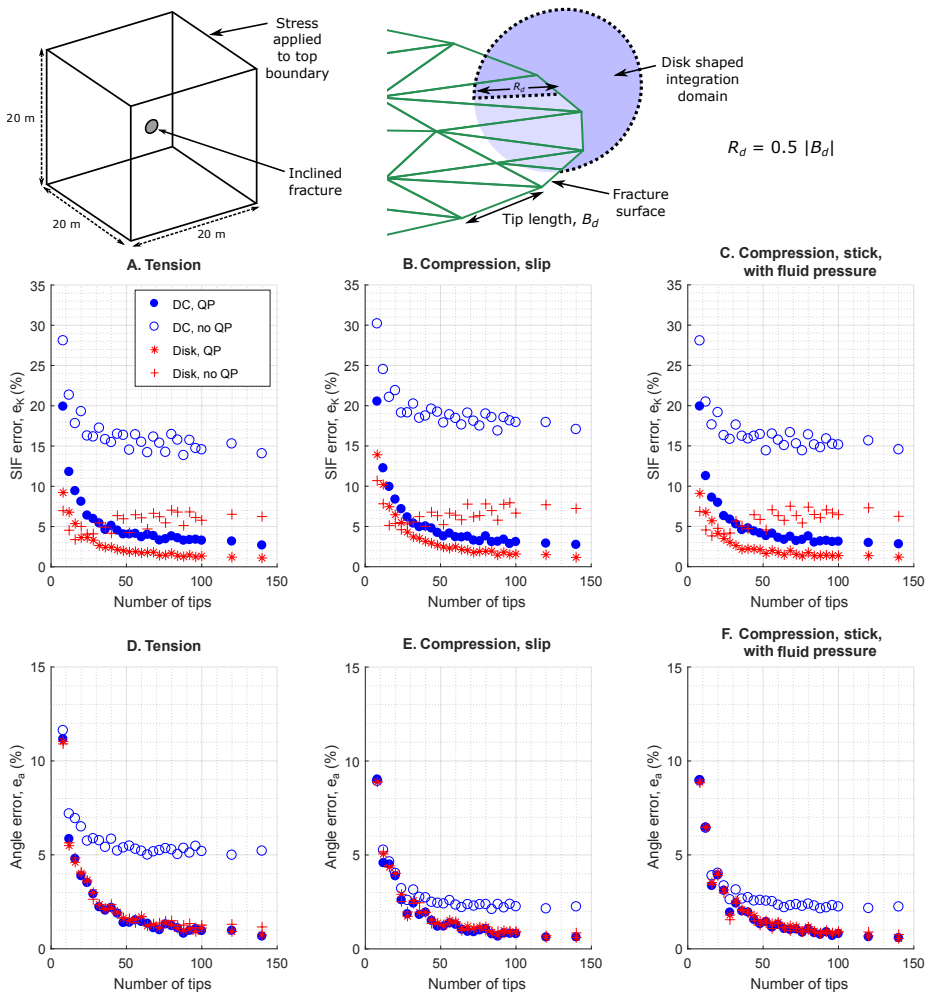


Figure 3: Stress intensity factor and propagation angle error for an inclined fracture under three stress states. Results are shown for the Displacement Correlation (DC) and the disk-shaped domain integral (Disk) methods, with and without quarter points elements (QP). The number of tips correlates with mesh density along the fracture tip, and linearly with the total number of elements in the domain. For 8 tip nodes, there are 1264 elements in the domain, and for 140 tip nodes, there are 22784 elements.

point elements consistently improve SIF accuracy in both methods. The propagation angle error is particularly small for fractures with more than 40 tips, especially given that this is the total error along the entire tip. Thus, fractures grown using coarse meshes will still produce accurate geometries. Furthermore, both SIF computation methods result in a very similar e_a, despite DC being

consistently less accurate, suggesting that in computationally expensive simulations, using DC provides a similar accuracy for fracture growth whilst saving significant computation time.

4. Mixed mode fracture growth

This section investigates growth of fractures under tension and compression. A circular flaw with no initial aperture is inclined at 45° to the principal stress direction, at the center of a 20×20×20 m cube. A principal stress of $\pm 1 \times 10^7$ Pa is applied in each step in the vertical axis for tension and compression respectively. In each step, $\Delta a_v = 0.1$ m, and $\beta_n = 2$. The fractures are grown alone, therefore the first step of the modified Paris law (Equation 8) does not affect their geometry. Stress intensity factor analytical solutions are not available for fractures with complex 3D surfaces. Instead, the fracture geometries are validated by comparison to experimental observations (Section 4.3).

4.1. Tension

Figure 4 shows a diagram of the volume containing the fracture, and the geometry of the fracture from two viewpoints, over 30 growth steps. In the first step, the fracture grows sharply away from its initial plane. The propagation angle changes smoothly along the tip, pointing in opposite directions at the very top and bottom. Over the following steps, the fracture grows at a similar angle as in the previous step, with a smaller change in angle over time, converging towards an angle perpendicular to the principal stress direction. This manner of growth matches the widely observed wing crack [*e.g.*, 73]. The fracture maintains its initially circular shape for three reasons. Firstly, the value of $\mathcal{G}_n$ relatively uniform along the tip, meaning similar Δa_n values are assigned using Equation 9. Secondly, on a non-circular tensile fracture, $\mathcal{G}_n$ varies such that propagation converges towards a circular shape [40]. Thirdly, as the growth

step number increases, K_I becomes progressively larger relative to the magnitudes of K_{II} and K_{III}, meaning φ tends towards zero and the fracture becomes increasingly planar and disc-shaped.

4.2. Compression

Figure 5 shows the growth of a fracture under compression over 30 steps. Similar to the tension case, the compressed fracture grows as a wing crack, orienting itself parallel to the maximum compressive principal stress direction. Similar geometries are widely observed in compression experiments, [*e.g.*, 74–76]. Even when rocks are under uniaxial compression, fractures still prefer to grow in the opening mode, curving towards an orientation parallel to the direction of compression [77]. In the first step, the fracture changes angle significantly away from its initial plane, with a smaller change in angle with each subsequent step. The fracture initially grows uniformly in all directions until the top and bottom tips of the fracture have become vertical. Once vertical, the top and bottom of the fracture grow much less, and the sides propagate instead, creating a horizontally elongated fracture.

In the later stages of growth under compression, the top and bottom of the fracture experience high in-plane shear, leading to K_{II} being much larger than K_I and K_{III}. This causes the propagation angle to alternate between two extremes, resulting in an alternating path of growth. In the limit where Δa_n tends towards zero, the path tends to be straighter. In Figure 5, this effect is attenuated by reducing the magnitude of K_{II} by half when evaluating the angle criterion. Without this adjustment, the fracture surface is not as smooth, but its overall shape is very similar to the attenuated case. This means that the initial growth angle deviates from the analytical angle (see Section 3), but ensures the overall shape of the fracture more closely resembles a wing crack. Similar adjustments to K values have been used in other models to ensure

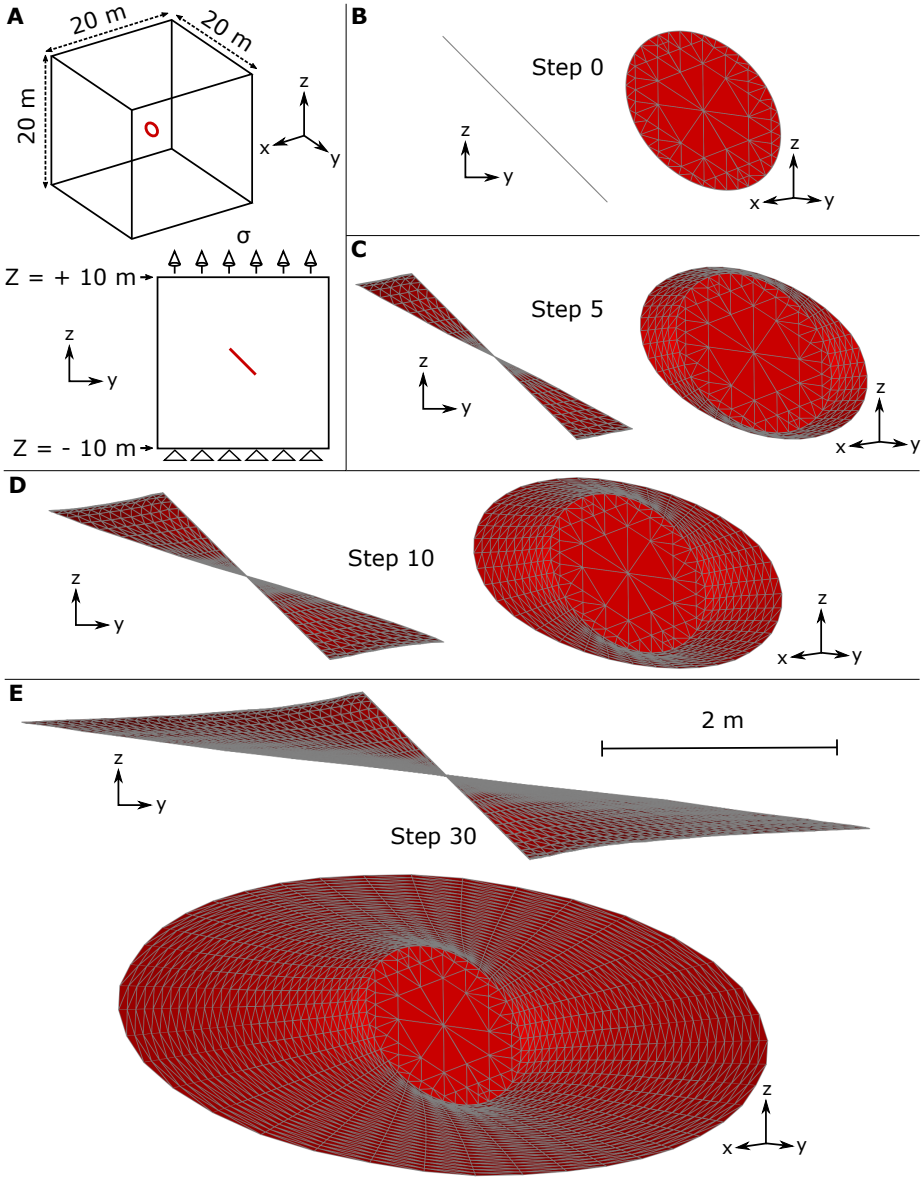


Figure 4: Isolated fracture growth under tension. A: Domain and boundary conditions, showing the initial fracture in red, from two orientations. B: Geometry of the initial fracture before growth (step 0). C, D, and E: Geometry of the fracture during growth at steps 5, 10, and 30 respectively. The fracture has 40 tip nodes, initial radius 1 m, placed with its centre at the centre of the domain (0, 0, 0), and is initially inclined at 45° to the direction of maximum tension. The maximum extension in each step (Δa_v) is 0.1 m. The stress applied to the $+z$ boundary is $\sigma = 1 \times 10^7$ Pa.

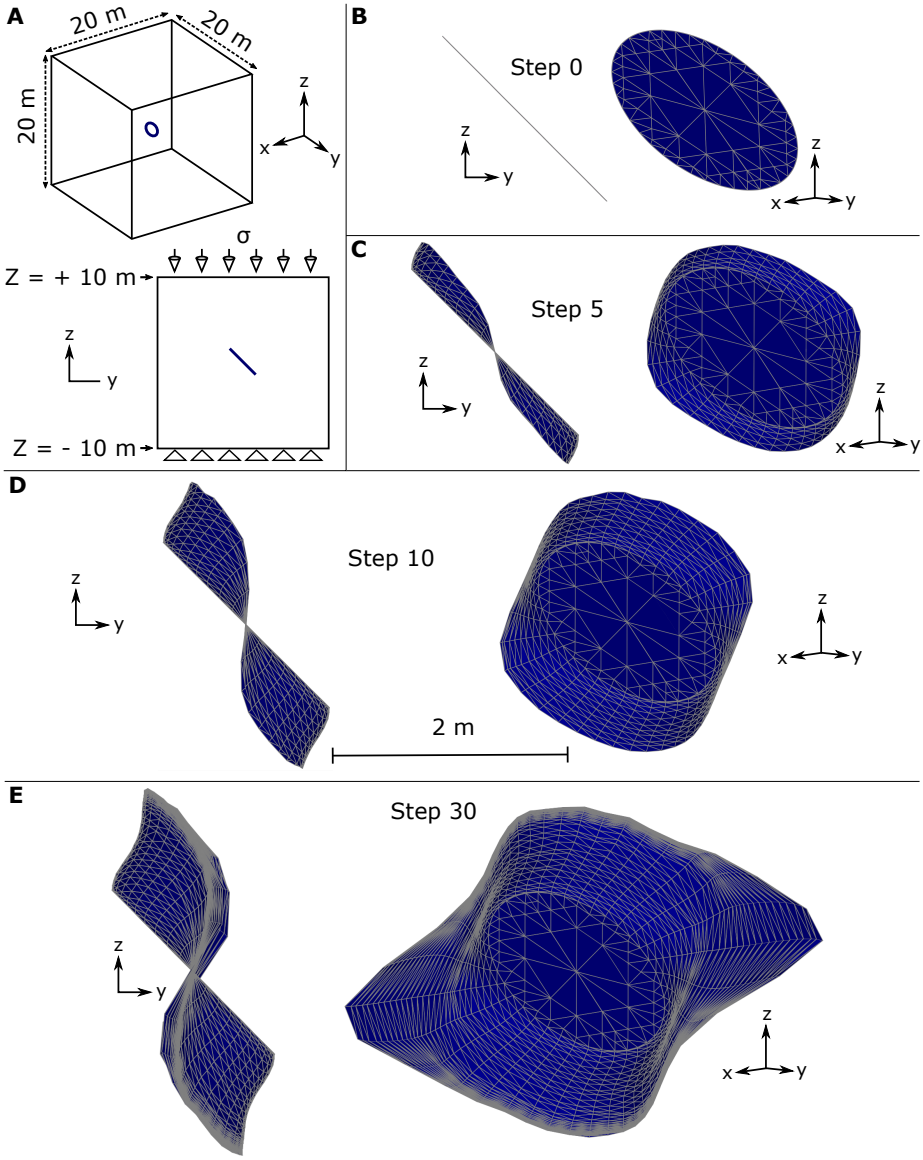


Figure 5: Isolated fracture growth under compression. A: Domain and boundary conditions, showing the initial fracture in blue, from two orientations. B: Geometry of the initial fracture before growth (step 0). C, D, and E: Geometry of the fracture during growth at steps 5, 10, and 30 respectively. The fracture has 40 tip nodes, initial radius 1 m, placed with its centre at the centre of the domain (0, 0, 0), and is initially inclined at 45° to the direction of maximum compression. The maximum extension in each step (Δa_v) is 0.1 m. The stress applied to the $+z$ boundary is $\sigma = 1 \times 10^7$ Pa. The friction coefficient between the fracture surfaces is 0, making K_I non-zero and allowing the faces of the fracture to slide past one another.

smooth fracture growth, *e.g.*, moving averages [57].

4.3. Comparison with experimental results

Figure 6 shows a further validation comparing cut-planes through the final three-dimensional geometries shown in Figures 4 and 5 to experimental two-dimensional wing crack paths [6, 74]. A single curve is created from the three-dimensional geometries by finding the intersection between the fracture and a plane through the x-z axes ($x = 0$, $z = 0$). The experimental results are not from unique experiments, rather, they are interpreted from outcrops and experiments with brittle materials [8, 77–82]. Therefore, Figure 6 is not a direct comparison calibrated to the same material properties, but a demonstration that the generated three-dimensional geometries are qualitatively similar to those found in experiments. The propagation angle in step 0 is validated quantitatively in Figure 3D-F.

These results show one of many possible vertical cut-planes, as any cut plane on the x-z plane could be visualised. Offsetting the plane would result in smaller initial flaw and different curvature. The orientation of stress shown by arrows in Figure 6A and C demonstrates that wing cracks orient themselves perpendicular to the direction of the minimum compressive stress. There are many differences in the mechanics of the growth between the cases, all of which are emergent properties of using a fracture mechanics based approach. Compression requires a progressively larger load to continue propagation, whereas a tensile fracture requires no additional stress, because a larger fracture acquires larger SIFs in tension as long as the stress magnitude remains the same. The location of maximum aperture also differs, with the whole fracture opening in tension [*e.g.*, 8], and only the most curved wings opening under compression [74].

There are many parameters in a quasi-static growth scheme which influence fracture growth. Figures 4 and 5 demonstrate typical growth for the cases of

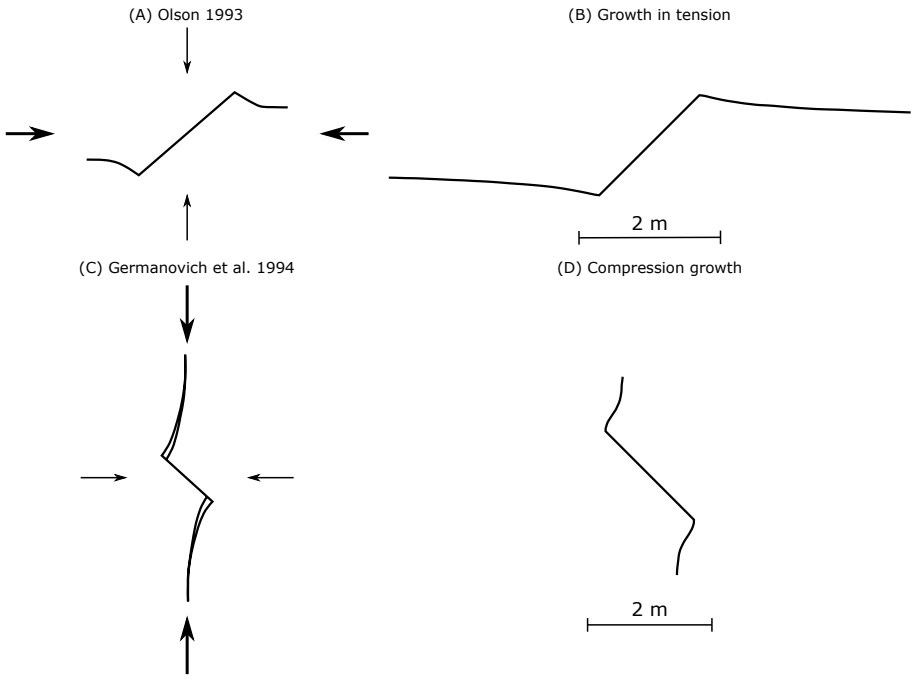


Figure 6: Comparison between experimental wing cracks in literature, and simulated inclined flaws under tension and compression in the present work. A: Figure 2A from Olson [6], demonstrating wing crack growth under tension. B: Tension fracture from Figure 4 in step 30, visualised as the intersection of a plane in the x-z axes. C: Figure 1A from Germanovich et al. [74], showing a fracture growing from an inclined flaw under uniaxial compression. D: Compression fracture from Figure 5 in step 30, visualised as the intersection of a plane in the x-z axes.

tension and compression, for relatively small Δa_v values, in order to validate growth over many steps. If $\mathcal{G}$ varies significantly along the tip, such as in the compression case, differences in Δa_v and N_f result in different fracture shapes. For example, if Δa_v is large, tips with lower values of $\mathcal{G}$ grow much less, leading to a more elongated fracture in the vertical axis. If N_f is increased, there are more tips amongst which the largest value of $\mathcal{G}_n$ can be chosen, leading to larger variations in growth along the fracture tip. Varying these parameters do not prevent growing fractures from converging towards accurate geometries if sufficient growth steps are simulated.

5. Growth of fracture arrays

Arrays containing five *en échelon* fractures are grown in tension to demonstrate how fracture interaction alters simultaneous growth. The fractures are separated by 1 m in the x and z axes at the centre of a 20 $\times$ 20 $\times$ 20 m cubic domain, with an initially circular shape with radius 1 m. They are aligned perpendicular to the direction of tension (z). The rock matrix has Young's modulus, Poisson's ratio, and K_{IC} of 20 GPa, 0.213, and 10^6 Pa m$^{1/2}$ respectively. The same tensile boundary condition shown in Figure 4A is used with a stress magnitude on the top boundary of 8 $\times$ 10^7 Pa. Arrays are visualised at their 34^{th} growth step in Figure 7, before boundary intersections occur, showing the tip loop at every other step, including the initial tip loop.

The geometric differences between the arrays result from changing β_f and β_n, as these values influence how variations in $\mathcal{G}_n$ determine extension lengths. High values of the exponents result in growth being more concentrated on fractures with higher $\mathcal{G}_f$, or fractures with higher $\mathcal{G}_n$ values. Variations in $\mathcal{G}_n$ in the present arrays are caused by three factors: interaction, fracture size, and fracture height. Interaction between fractures reduces $\mathcal{G}_n$ at overlapped tips due to stress shielding [5]. Larger fractures acquire higher stresses and $\mathcal{G}_n$ values. The fractures closer to the $+z$ boundary acquire slightly higher $\mathcal{G}_n$ values, because the $-z$ boundary is fixed and the $+z$ boundary in stressed, meaning are relatively higher displacements towards the top of the domain, which are sampled to calculate the SIFs and $\mathcal{G}_n$ (see Section 2.4.1). This variation is small and only affects the growth pattern if the exponents are large, but can cause arrays to become asymmetric.

Figure 7A-D are four different viewpoints of array 1, grown with $\beta_f = 0.35$ and $\beta_n = 2$. Fracture growth is significantly affected by mechanical interaction. Much less extension occurs where fractures are overlapped. Most growth occurs

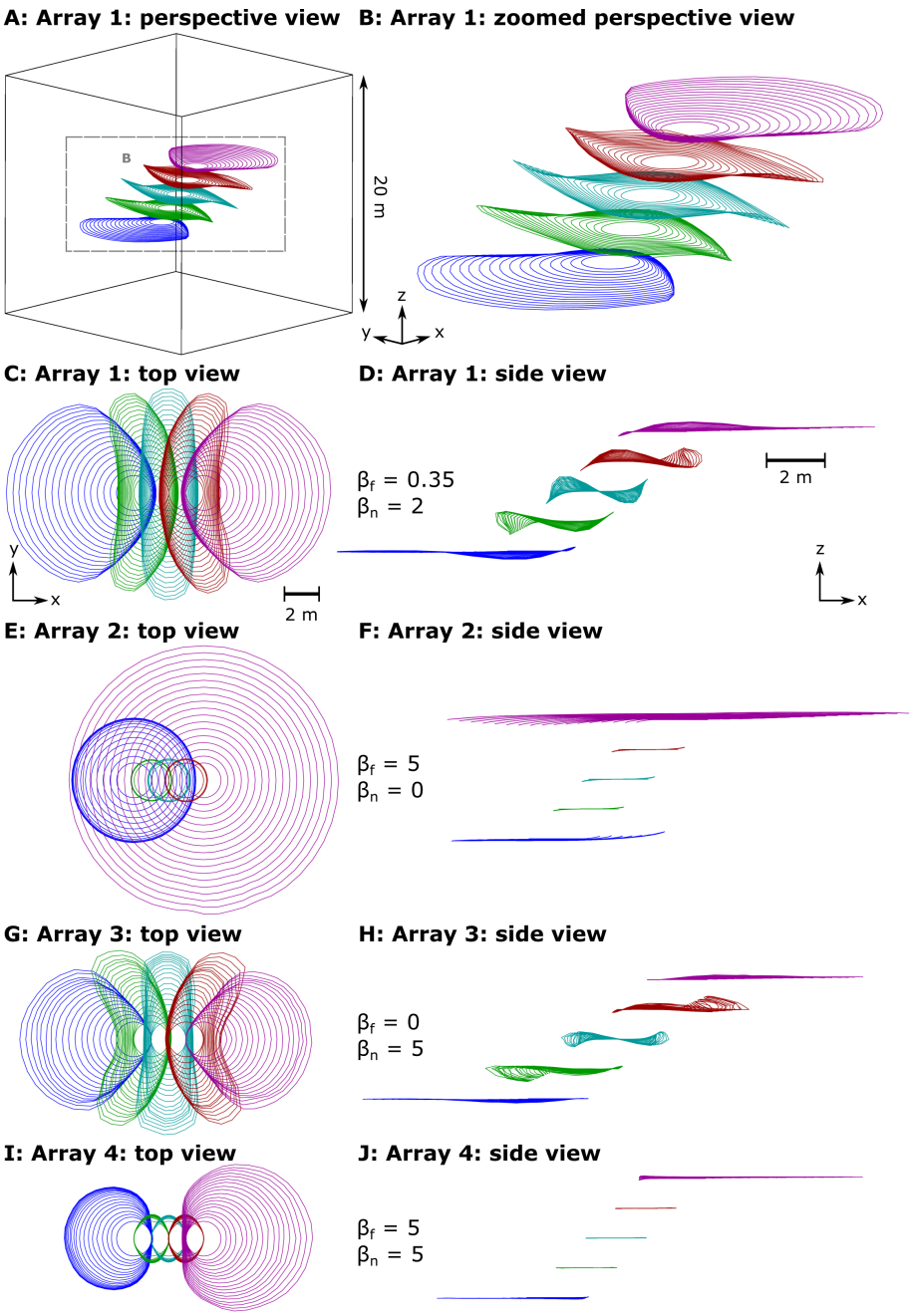


Figure 7: Four fracture arrays, grown from the same initial flaws in tension with different values of β_f and β_n, viewed from the top and side. Each array is shown after 34 growth steps. A-D use $\beta_f = 0.35$ and $\beta_n = 2$, E and F use $\beta_f = 5$ and $\beta_n = 0$, G and H use $\beta_f = 0$ and $\beta_n = 5$, and I and J use $\beta_f = 5$ and $\beta_n = 5$.

on the top and bottom fractures in the array, particularly on the side which is unaffected by other fracture's stress shadow zones [5]. All fractures grow along the y axis where there is more space for part of the tip to grow outside of the other fracture's stress shadows, elongating the central three fractures. The fractures become curved when overlapped, with the angle of curvature varying smoothly along the tip. The intermediate value of β_n means the local variation in $\mathcal{G}_n$ has a relatively large control on the growth at each tip.

The relationship between the fracture growth exponent and interaction patterns has been noted by other authors [6, 12, 36]. Arrays 2 to 4 in Figure 7 demonstrate the effect of the exponents in the modified two step Paris-type law introduced in Section 2.4.4 on growth. The same initial array in grown in Figure 7A is used again, with β_f and β_n values of 0 and 5, respectively. Setting either β_f and β_n to zero means the associated step in the modified two step Paris-type growth law does not affect the growth extent. An exponent of 5 in a power law creates a steep curve, where only fractures or tips with the highest values of $\mathcal{G}_n$ will propagate [83].

In array 2 (Figure 7E and F), $\beta_f = 5$ and $\beta_n = 0$. Therefore, the highest value of $\mathcal{G}_n$ on each fracture determines a uniform extension length, and the local variation in the value of $\mathcal{G}_n$ on each tip does not change the extension length ($\Delta a_f = \Delta a_n$). This produces a significantly different growth pattern to array 1, with much less activation of the inner fractures. The top fracture (purple) grows at the maximum extension length throughout the 34 growth steps, eventually overlapping the other fractures. This fracture acquires a slightly higher value of $\mathcal{G}_n$ compared to the others, because it does not overlap with as many other fractures initially, and because the boundary condition results in higher values of displacement closer to the $+z$ boundary. The lower four fractures stop growing when the larger fracture begins to overlap them. This extinction of growth

is particularly clear on the bottom (blue) fracture, which initially has similar growth to the top fracture, but after 16 steps (when the top fracture begins to overlap it), it grows with a smaller extension length per step and eventually stops. Very little curvature develops, except in the bottom and top fractures which curve vertically at one side.

In array 3 (Figure 7G and H), $\beta_f = 0$ and $\beta_n = 5$, meaning all fractures have the same maximum extension length regardless of their largest $\mathcal{G}_n$ value, and each tip has its own unique Δa_n. This results in growth occurring more evenly across the five fractures, with their surface areas being similar in the final step. The local variation in the extension of each fracture tip means the fractures tend to grow into space where they do not overlap. More vertical curvature arises than the $\beta_f = 5$, $\beta_n = 0$ case, but less than in Figure 7 because growth in stress shadow zones is relatively more discouraged, which is a result of using a higher value of β_n.

In array 4 (Figure 7I and J), $\beta_f = \beta_n = 5$, meaning both steps of the modified Paris-type law have a significant effect on growth, and extension is strongly concentrated on fractures and tips with the highest $\mathcal{G}_n$. The results show an array with much less growth, in terms of total additional surface area added per step, for the same number of growth steps as the other cases. The strong preference for growth to only occur where $\mathcal{G}_n$ is very close to $\mathcal{G}_v$ leads to very little growth on the middle fractures, even when these fractures do not overlap as much as the other cases. Similar to array 2, most of the growth happens on the top fracture because displacements are larger nearer the top of the domain.

Figure 7 shows that the effect of the growth rate exponent on growth during interaction is significant. The key interaction effects in the growth of these arrays are the shadow zone effects, reducing the extent of each fracture's growth, and

the curving of fractures towards or away from one another. Higher values of the exponent tend to increase the shadow zone effect, and decrease the curvature which arises. Higher values of the growth exponent (*e.g.,* 30 and 60 [67]) would therefore concentrate growth significantly towards the most critically stressed fractures and fracture tips.

5.1. Outcrop visualisation of arrays

Figure 8 shows five fractures grown from initial flaws arranged in a spiral, rather than an aligned array as show in Figure 7. The material properties and boundary conditions match those used in Section 5, with $\beta_f = 0.35$ and $\beta_n = 2$. The array is visualised in three-dimensions (Figure 8 A and B) and by their intersection with four cut-planes (C-F). The cut-plane visualisation simulates how the array would appear in outcrop, and demonstrates that the apparent curvature of the fractures varies significantly depending on the location and orientation of the cut-plane. Hooking tips are visible in most planes, with varied shapes depending on the location of the intersecting plane. Plane 1 does not intersect the initial flaw surfaces of the middle three fractures, leading to slanted traces. Without context of the full fracture array geometry, this rotation could be interpreted as a rotation of the material between the larger two fractures, as identified in relay ramps in outcrop [84]. Plane 4 (Figure 8F) does not intersect the fourth fracture (counted from the top of the array), but its presence could be inferred due to the curvature on the third and fifth fractures.

6. Growth of fracture networks

This section presents an example of a dense fracture network grown using the present methodology. The term 'geomechanical discrete fracture network' (GDFN) is adopted in this work to describe the network [12] because its properties are the result of the mechanical deformation driving the growth of frac-

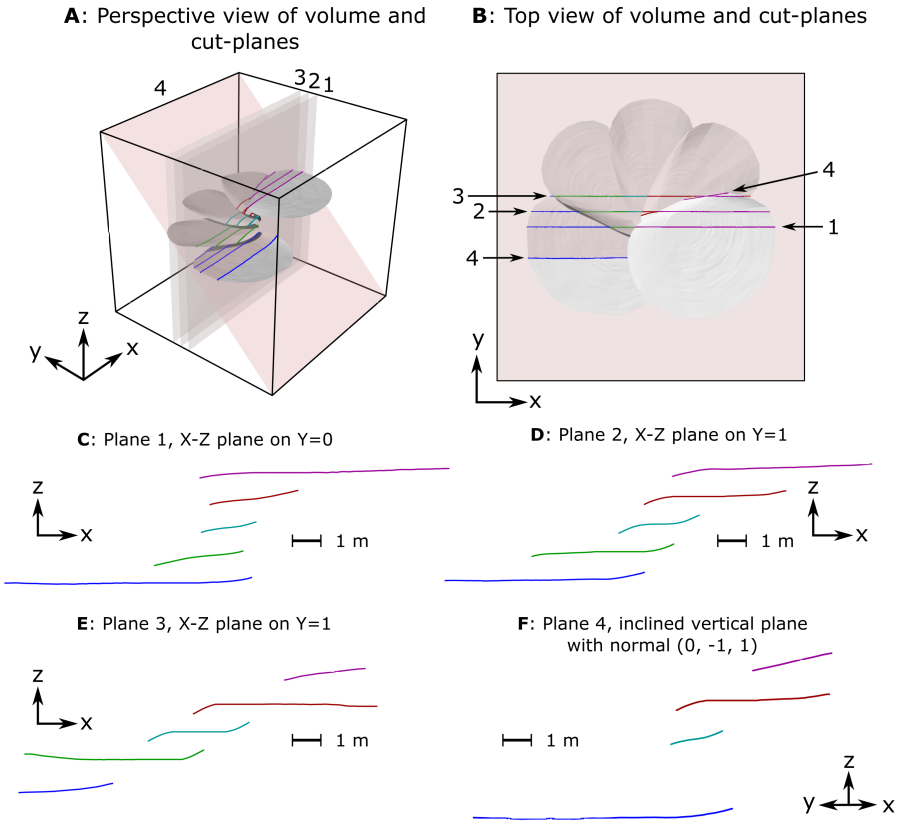


Figure 8: A fracture array grown from initial flaws arranged in a spiral. A and B show perspective and top-down views of the volume, including both the visualisation planes as transparent surfaces, and the fractures as opaque surfaces. The trace of each fracture is also included and coloured using the colour scheme from Figure 7. C, D, E and F show the traces from each of the intersection planes. Cut-plane traces are shown from a perspective perpendicular to the plane.

tures in the domain. The domain initially contains sixty disk-shaped fractures, randomly placed in the central region of the domain. Fifty of these fractures (referred to as 'set one' fractures and shown in red) are parallel to the $x - y$ plane and have an initial radius of 0.5 m. Ten of the fractures ('set two', shown in blue) are inclined with their planes normal to the vector (4, 5, 1), and an initial radius of 2.5 m. These two fractures fractures represent fractures from different phases of deformation, with set one fractures optimally inclined for

growth. Due to their inclination, set two fractures do not grow until stress at their tips increases, which as the simulation progresses, occurs when the fracture intensity increases due to growth in fracture set one.

Material properties for hard rocks (*e.g.*, granite) were chosen to make the resulting network particularly relevant to radioactive waste disposal and other deep rock applications. The rock matrix has Young's modulus of 20×10^9 Pa, Poisson's ratio of 0.2 [85], and K_{IC} of 1×10^6 Pa m$^{1/2}$ [62]. A tensile stress of 2×10^6 Pa is applied at the top boundary. Fracture tips can extend by up to 2 m each step (Δa_v), and the domain stops growing when no further surfaces are added (*i.e.*, no further tips meet the failure criterion). Fracture growth exponents of $\beta_f = 0.35$ and $\beta_n = 2$ are used, ensuring that many fractures activate and grow concurrently, whilst still being significantly influenced by fracture interaction, as observed in Figure 7. Whilst measurements of growth exponents in geological materials tend to be higher [67], higher values result in much less growth per step, significantly increasing the computational cost of generating high density networks. SIFs are calculated using the DC method to reduce the overall computational cost of growing the network.

The full network is grown for 33 steps, with the initial state and steps 4 and 8 shown in Figure 9. In the early steps, a rapid increase in fracture density occurs as the initially flat set one fractures grow in their plane. Growth of set two fractures is not as rapid as they acquire lower values of $\mathcal{G}_n$ due to their initial inclination. They activate more where they are close to other fractures (due to stress amplification), and new surfaces re-orient towards the $x-y$ plane, perpendicular to the direction of tension. Many fractures terminate growth once intersected, with some X intersections occurring when fractures intersect in the initial state. Connected pathways between opposite boundaries have formed by the 4^{th} growth step, creating a percolating network in the x and y planes.

Most fracture tips experience stress shielding, due to the density of the network, leading to highly varied fractures shapes in step 8.

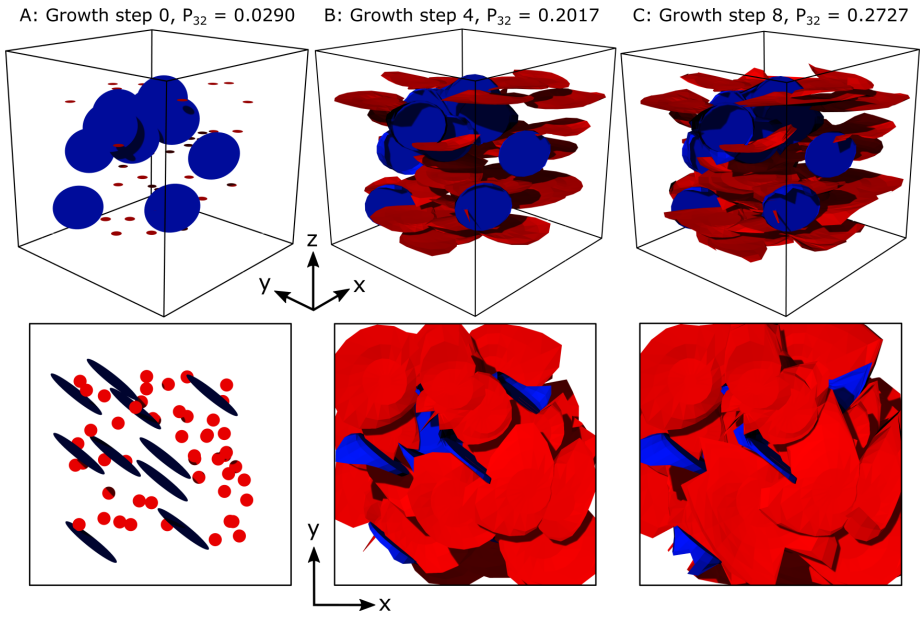


Figure 9: Geometry of a geomechanically grown discrete fracture network at three growth steps (0, 4, and 8). Sixty initial fractures are grown in a 20 × 20 × 20 m cube. Fifty of the fractures are initially flat with a radius of 0.5 m (coloured red), and ten are inclined with a radius of 2.5 m (coloured blue).

Figure 10 shows the GDFN in its 33$^{\text{rd}}$ growth step. In this step, the fracture intensity of the network has increased by approximately fifteen times. Most of this growth occurs in the early steps, where there is more space available for fracture growth. In later growth steps, most fracture tips become intersected against the boundaries or other fractures, reducing the surface area added in each step. Fractures from set one have the most variable surface areas, between 10.04 and 149.7 m^2, with a median of 53.0 m^2. Set two fractures have a similar median surface area (49.1 m^2) and a smaller range (39.4 - 105.4 m^2). Fracture propagation mostly occurs in the plane of the minimum principal stress, meaning the final network is highly anisotropic. Multiple connected pathways form between the opposing x and y boundaries, and no percolating path forms in the

vertical direction.

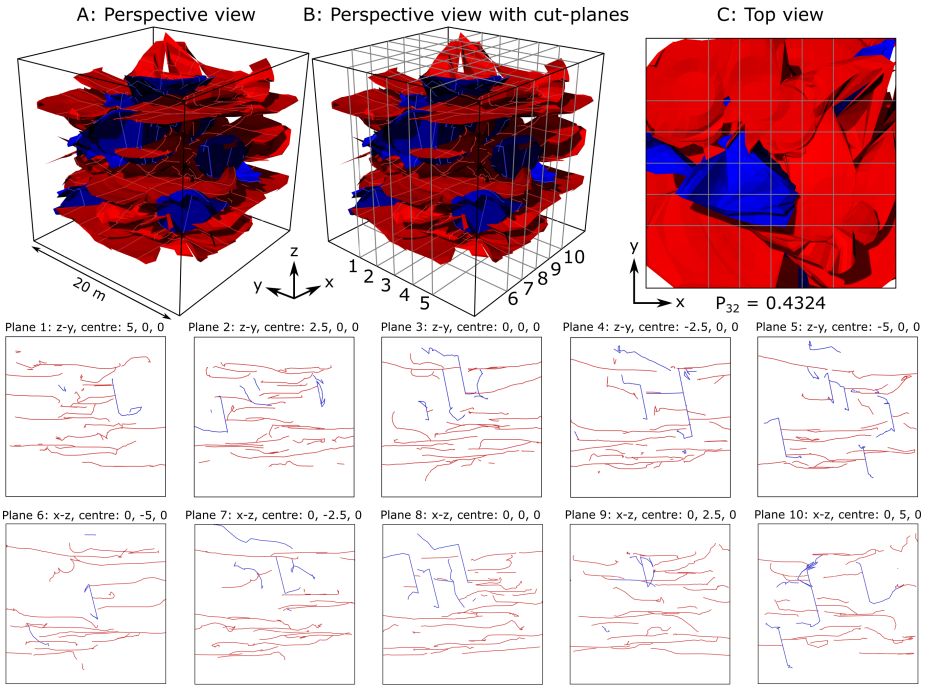


Figure 10: Three-dimensional geomechanically generated fracture network after 33 growth steps. A, B, and C show perspective and top-down views of the dataset. The intersection between cut-planes and the fractures are shown in planes 1 to 10, coloured by fracture set (red fractures are in set one, blue fractures are in set two). Three-dimensional views have a light source to the left of the viewpoint, meaning some surfaces are shaded.

To demonstrate the internal structure of the network, Figure 10 shows ten different cut-planes through the domain. The cut-planes are arranged around the central region of the domain, and therefore include the regions where initial flaws were inserted, and where the domain has the highest fracture density. The cut-planes reveal the complex surfaces of the fractures, and each plan has similar properties.

Horizontal set one fractures grow to cross up to half of the domain. Inclined set two fractures are present all in the cut-planes, and undergo significant changes in their propagation angle during growth. In some planes, fractures curve back onto themselves and terminate, both from set one and set two (*e.g.*,

planes 1 and 7). Some of these fracture paths may be the result of fracture-planes intersections at angles which enhance the curvature. In most cases, these paths are the results of fractures continually re-orienting themselves towards the direction which maximises stress at their tips, *i.e.*, avoiding regions of stress shielding.

Many fracture intersections and close fracture surfaces can be observed. Relatively few fractures cross-cut one another, with some exceptions visible in cut-planes 3, 9, and 10. All the cut-planes feature some fracture traces which are curved, and some traces are jagged with sharp changes in direction. Planes 3, 7, and 8 have clear percolation paths between the two sides of the domain, and it is reasonable to conclude that fractures that are close to intersecting would likely intersect in other possible cut-planes.

7. Discussion

The present growth algorithm produces highly realistic growth in three dimensions, demonstrated by the SIF validation, comparisons to experimental cases, and interaction patterns in arrays and networks. Accurately reproducing specific growth experiments would be challenging due to sample heterogeneity. Fractures growing simultaneously in this work tend to activate together, whereas in real experiments, growth may be localised onto one fracture at a time [*e.g.*, 86]. Fracture analysis benefits greatly from visualising fully three-dimensional fracture surfaces, where multiple cut-plane traces can be sampled to understand how the fracture would appear in experiments or outcrops.

The modified two step Paris-type law captures the variation in extension between different fractures and fracture tips within a growing network. Fractures must have grown concurrently in order to create the patterns that are observed in outcrops, and to create curvature that arises during stress field

re-orientation caused by fracture interaction [7–9]. Higher values of β_n and β_f generate fracture patterns where growth is more concentrated on the most energetic fractures and fracture tips (see Figures 7 and 8). If a single step Paris-type law was used to model growth in a complex domain, fractures would be unlikely to activate widely, and growth would be highly focused on relatively few critically stressed fracture tips. For a domain in tension, bias towards the most energetic tips would become more significant when these fractures become larger, making the generation of densely fractured domains highly computationally expensive. By separately defining a maximum extension per fracture with the first step of the modified Paris-type law, fractures can grow simultaneously and competitively, experiencing interaction effects during growth. Furthermore, the present method enables concurrent growth without explicit time increments in growth steps, a feature which would add significant computational time requirements and complexity to fracture growth. By exploring how quasi-static fracture growth is affected by different growth parameters, particularly the maximum extension length and growth exponents, this work highlights that further work should explore how these parameters can be selected to grow the most realistic fracture patterns.

The grown GDFN presented in Section 6 is significant in the context of discrete fracture network models. The processes driving its generation are neither stochastic nor pseudo-mechanical, rather, they are based on the physics of fracture growth. Therefore, realistic features of subsurface networks emerge as a result of the distribution of stress and interaction between concurrently growing fractures. Despite being initialised with a stochastic distribution of fractures, the final properties of the GDFN are determined by the tensile boundary condition, causing the initially sparse and isotropic network to become well connected, dense, and highly anisotropic. The P_{32} fracture intensity of the final network

(0.4324 m^{-1}) is on the same order of magnitude as intensities as fracture sets observed in deep subsurface networks in hard rock environments. Cvetkovic et al. [87] analysed a network containing three fractures sets with estimated P_{32} values of 0.18, 0.26, and 0.85 m^{-1}. Follin et al. [88] examined several fracture zones and depth intervals in Forsmark, Sweden, where the P_{10} of observed open fractures ranges between 0.535 and 3.17 m^{-1}. These comparisons demonstrate the present methodology can readily be used to simulate fracture networks at sufficient detail to match real fracture intensities. Additional realism can be introduced to the generation of GDFNs by imposing a more complex stress history on the domain, and by further exploring the effect of mechanical parameters on network growth, particularly β_f and β_n, as these effect how fractures interact during growth.

8. Conclusions

A novel finite-element based, quasi-static, discrete fracture growth method is presented, validated, and applied to growth of fractures in *en échelon* arrays and networks. Stress Intensity Factors (SIFs) are used to evaluate growth criteria which govern mixed mode fracture growth. The accuracy of the method is demonstrated through quantification of SIF and propagation angle errors (Section 3), and isolated fracture growth in tension and compression (Section 4). A novel modified Paris-type law models the relative growth rate of different fractures growing quasi-statically. Fracture growth exponents are shown to be important in influencing how fractures grow concurrently. Fracture interaction suppresses growth in stress shadow zones and alters propagation angles non-uniformly along fracture tips, producing complex non-planar surfaces. The method is applied to grow a dense, complex fractured domain, generating a geomechanical discrete fracture network (GDFN). Realistic processes which arise

during the development of the GDFN include anisotropic non-planar surface growth, stress amplification and shielding, and fracture activation and deactivation. The resulting network is well connected and has similar densities to deep natural fracture networks in hard rock environments. GDFNs provide models of the subsurface which are formed based on the physics of fracture growth and interaction. Furthermore, they can be generated to qualitatively and quantitatively model specific subsurface environments, by incorporating estimated initial flaw distributions, the mechanical conditions imposed by regional tectonic events and present *in situ* stresses.

9. Acknowledgments

The authors thank the Natural Environment Research Council, Radioactive Waste Management Limited, and Environment Agency for the funding received for the HydroFrame project, NE/L000660/1, through the Radioactivity and the Environment (RATE) programme, and the European Commission for partially funding this work through the TRUST Collaborative Project, 309067. Adriana Paluszny thanks the Royal Society for partially funding this research through fellowship UF160443.

References

[1] R. Munier. Statistical analysis of fracture data, adapted for modelling discrete fracture networks (version 2). Technical Report R-04-66, Swedish Nuclear Fuel and Waste Management Company (SKB), 2004.

[2] Ronald Nelson. *Geologic analysis of naturally fractured reservoirs.* Gulf Professional Publishing, 2001.

[3] Rafael March, Florian Doster, and Sebastian Geiger. Assessment of CO_2 Storage Potential in Naturally Fractured Reservoirs With Dual-

822 Porosity Models. *Water Resources Research*, 54(3):1650–1668, 2018. doi:
823 10.1002/2017WR022159.

824 [4] O. Kolditz. Modelling flow and heat transfer in fractured rocks: Conceptual
825 model of a 3-D deterministic fracture network. *Geothermics*, 24(3):451–470,
826 1995. ISSN 03756505. doi: 10.1016/0375-6505(95)00020-Q.

827 [5] Robin N. Thomas, Adriana Paluszny, and Robert W. Zimmerman. Quan-
828 tification of fracture interaction using stress intensity factor variation maps.
829 *Journal of Geophysical Research: Solid Earth*, 122(10):7698–7717, 2017.

830 [6] Jon E. Olson. Joint pattern development: Effects of subcritical crack
831 growth and mechanical crack interaction. *Journal of Geophysical Research*,
832 98(B7):12251, 1993. ISSN 0148-0227. doi: 10.1029/93JB00779.

833 [7] P. Segall. Formation and growth of extensional fracture sets. *Geologi-*
834 *cal Society of America Bulletin*, 95(4):454–462, 1984. doi: 10.1130/0016-
835 7606(1984)95¡454:FAGOEF¿2.0.CO;2.

836 [8] D. D. Pollard, P. Segall, and P. T. Delaney. Formation and
837 interpretation of dilatant echelon cracks. *Geological Society of*
838 *America Bulletin*, 93(12):1291–1303, 1982. doi: 10.1130/0016-
839 7606(1982)93¡1291:FAIODE¿2.0.CO;2.

840 [9] Juliette Lamarche, Arezki Chabani, and Bertrand DM Gauthier. Dimen-
841 sional threshold for fracture linkage and hooking. *Journal of Structural*
842 *Geology*, 108:171–179, 2018.

843 [10] Ted L Anderson and TL Anderson. *Fracture mechanics: fundamentals and*
844 *applications (fourth edition)*. CRC press, 2017.

845 [11] Bryan S.A. Tatone and Giovanni Grasselli. Characterization of the effect of
846 normal load on the discontinuity morphology in direct shear specimens us-

ing X-ray micro-CT. *Acta Geotechnica*, 10(1):31–54, 2014. ISSN 18611133. doi: 10.1007/s11440-014-0320-5.

[12] Qinghua Lei, John-Paul Latham, and Chin-Fu Tsang. The use of discrete fracture networks for modelling coupled geomechanical and hydrological behaviour of fractured rocks. *Computers and Geotechnics*, 85:151–176, 2017. ISSN 0266-352X. doi: 10.1016/j.compgeo.2016.12.024.

[13] Brice Lecampion, Andrew Bunger, and Xi Zhang. Numerical methods for hydraulic fracture propagation: A review of recent trends. *Journal of Natural Gas Science and Engineering*, 49:66–83, 2018. doi: 10.1016/j.jngse.2017.10.012.

[14] Rongxin Zhou, Zhenhuan Song, and Yong Lu. 3D mesoscale finite element modelling of concrete. *Computers and Structures*, 192:96–113, 2017. ISSN 00457949. doi: 10.1016/j.compstruc.2017.07.009.

[15] Saeed Salimzadeh, Adriana Paluszny, and Robert W. Zimmerman. Three-dimensional poroelastic effects during hydraulic fracturing in permeable rocks. *International Journal of Solids and Structures*, 108:153–163, 2017. ISSN 00207683. doi: 10.1016/j.ijsolstr.2016.12.008.

[16] Timon Rabczuk. Computational methods for fracture in brittle and quasi-brittle solids: State-of-the-art review and future perspectives. *International Scholarly Research Notices: Applied Mathematics*, 97:531–550, 2013. doi: 10.1155/2013/849231.

[17] Y. Jiang, T. E. Tay, L. Chen, and Y. W. Zhang. Extended finite element method coupled with face-based strain smoothing technique for three-dimensional fracture problems. *International Journal for Numerical Methods in Engineering*, 102(13):1894–1916, 2015. ISSN 00295981. doi: 10.1002/nme.4878.

[18] Jean H. Prévost and N. Sukumar. Faults simulations for three-dimensional reservoir-geomechanical models with the extended finite element method. *Journal of the Mechanics and Physics of Solids*, 86:1–18, 2016. ISSN 00225096. doi: 10.1016/j.jmps.2015.09.014.

[19] Chunfang Meng, Frantz Maerten, and David D. Pollard. Modeling mixed-mode fracture propagation in isotropic elastic three dimensional solid. *International Journal of Fracture*, 179(1-2):45–57, 2013. ISSN 03769429. doi: 10.1007/s10704-012-9771-6.

[20] X. Peng, E. Atroshchenko, P. Kerfriden, and S.P.A. Bordas. Isogeometric boundary element methods for three dimensional static fracture and fatigue crack growth. *Computer Methods in Applied Mechanics and Engineering*, 316:151–185, 2017. ISSN 00457825. doi: 10.1016/j.cma.2016.05.038.

[21] Huiying Tang, Philip H. Winterfeld, Yu Shu Wu, Zhao Qin Huang, Yuan Di, Zhengfu Pan, and Juncheng Zhang. Integrated simulation of multi-stage hydraulic fracturing in unconventional reservoirs. *Journal of Natural Gas Science and Engineering*, 36:875–892, 2016. ISSN 18755100. doi: 10.1016/j.jngse.2016.11.018.

[22] Dharmendra Kumar and Ahmad Ghassemi. A three-dimensional analysis of simultaneous and sequential fracturing of horizontal wells. *Journal of Petroleum Science and Engineering*, 146:1006–1025, 2016. ISSN 09204105. doi: 10.1016/j.petrol.2016.07.001.

[23] Michael J. Borden, Thomas J.R. Hughes, Chad M. Landis, and Clemens V. Verhoosel. A higher-order phase-field model for brittle fracture: Formulation and analysis within the isogeometric analysis framework. *Computer Methods in Applied Mechanics and Engineering*, 273:100–118, 2014. ISSN 00457825. doi: 10.1016/j.cma.2014.01.016.

[24] A. Lisjak and G. Grasselli. A review of discrete modeling techniques for fracturing processes in discontinuous rock masses. *Journal of Rock Mechanics and Geotechnical Engineering*, 6(4):301–314, 2014. ISSN 16747755. doi: 10.1016/j.jrmge.2013.12.007.

[25] Mijo Nikolic and Adnan Ibrahimbegovic. Rock mechanics model capable of representing initial heterogeneities and full set of 3D failure mechanisms. *Computer Methods in Applied Mechanics and Engineering*, 290:209–227, 2015. ISSN 00457825. doi: 10.1016/j.cma.2015.02.024.

[26] Jabrane Hamdi, Luc Scholtès, Mountaka Souley, and Marwan Al Heib. Effect of discretization at laboratory and large scales during discrete element modelling of brittle failure. *International Journal of Rock Mechanics and Mining Sciences*, 100:48–61, 2017. ISSN 13651609. doi: 10.1016/j.ijrmms.2017.10.022.

[27] Branko Damjanac and Peter Cundall. Application of distinct element methods to simulation of hydraulic fracturing in naturally fractured reservoirs. *Computers and Geotechnics*, 71: 283–294, 2016. doi: 10.1016/j.compgeo.2015.06.007. URL `http://dx.doi.org/10.1016/j.compgeo.2015.06.007`.

[28] Qinghua Lei, John-Paul Latham, Chin-Fu Tsang, Jiansheng Xiang, and Philipp Lang. A new approach to upscaling fracture network models while preserving geostatistical and geomechanical characteristics. *Journal of Geophysical Research: Solid Earth*, 120(7):4784–4807, 2015. ISSN 21699313. doi: 10.1002/2014JB011736.

[29] Chao Jiang, Gao Feng Zhao, and Nasser Khalili. On crack propagation in brittle material using the distinct lattice spring model. *International*

Journal of Solids and Structures, 118-119:1339–1351, 2017. ISSN 00207683. doi: 10.1016/j.ijsolstr.2017.04.024.

[30] Chengzeng Yan, Yu-Yong Jiao, and Hong Zheng. A fully coupled three-dimensional hydro-mechanical finite discrete element approach with real porous seepage for simulating 3D hydraulic fracturing. *Computers and Geotechnics*, pages 1–17, 2017. ISSN 0266352X. doi: 10.1016/j.compgeo.2017.10.008.

[31] Saeed Salimzadeh, Tomoya Usui, Adriana Paluszny, and Robert W. Zimmerman. Finite element simulations of interactions between multiple hydraulic fractures in a poroelastic rock. *International Journal of Rock Mechanics and Mining Sciences*, 99(September):9–20, 2017. ISSN 13651609. doi: 10.1016/j.ijrmms.2017.09.001.

[32] Shikou Yang, Maosen Cao, Xuhua Ren, Guowei Ma, Jixun Zhang, and Haijun Wang. 3D crack propagation by the numerical manifold method. *Computers and Structures*, 194:116–129, 2018. ISSN 00457949. doi: 10.1016/j.compstruc.2017.09.008.

[33] S. M. Barhli, L. Saucedo-Mora, M. S.L. Jordan, A. F. Cinar, C. Reinhard, M. Mostafavi, and T. J. Marrow. Synchrotron X-ray characterization of crack strain fields in polygranular graphite. *Carbon*, 124:357–371, 2017. ISSN 00086223. doi: 10.1016/j.carbon.2017.08.075.

[34] Saeed Salimzadeh, Adriana Paluszny, Hamidreza M. Nick, and Robert W. Zimmerman. A three-dimensional coupled thermo-hydro-mechanical model for deformable fractured geothermal systems. *Geothermics*, 71(September 2017):212–224, 2018. ISSN 03756505. doi: 10.1016/j.geothermics.2017.09.012.

[35] Seif Eddine Hamdi, Rostand Moutou Pitti, and Frédéric Dubois. Temperature variation effect on crack growth in orthotropic medium: Finite element formulation for the viscoelastic behavior in thermal cracked wood-based materials. *International Journal of Solids and Structures*, 115-116: 1–13, 2017. ISSN 00207683. doi: 10.1016/j.ijsolstr.2016.09.019.

[36] Carl E. Renshaw and David D. Pollard. Numerical simulation of fracture set formation: A fracture mechanics model consistent with experimental observations. *Journal of Geophysical Research*, 99(B5):9359–9372, 1994. doi: 10.1029/94JB00139.

[37] Zeno G. Philip, James Jennings, Jon E. Olson, Stephen Laubach, and Jon Holder. Modeling Coupled Fracture-Matrix Fluid Flow in Geomechanically Simulated Fracture Networks. In *Society of Petroleum Engineers Annual Technical Conference and Exhibition*, volume 8, 2005. doi: 10.2118/77340-PA.

[38] Adriana Paluszny and Stephan K. Matthäi. Impact of fracture development on the effective permeability of porous rocks as determined by 2-D discrete fracture growth modeling. *Journal of Geophysical Research*, 115(B2):1–18, 2010. ISSN 0148-0227. doi: 10.1029/2008JB006236.

[39] Hans A Richard, Alexander Eberlein, and Nils-H Schirmeisen. Experiments on cracks under spatial loading. In *13^{th} International Conference on Fracture*, 2013.

[40] Véronique Lazarus. Brittle fracture and fatigue propagation paths of 3D plane cracks under uniform remote tensile loading. *International Journal of Fracture*, 122(1-2):23–46, 2003. ISSN 03769429. doi: 10.1023/B:FRAC.0000005373.73286.5d.

[41] P. Gupta and C. A. Duarte. Simulation of non-planar three-dimensional hydraulic fracture propagation. *International Journal for Numerical and Analytical Methods in Geomechanics*, 38:1397–1430, 2014. ISSN 03639061. doi: 10.1002/nag.2305.

[42] P. O'Hara, C. A. Duarte, and T. Eason. A two-scale generalized finite element method for interaction and coalescence of multiple crack surfaces. *Engineering Fracture Mechanics*, 163:274–302, 2016. doi: 10.1016/j.engfracmech.2016.06.009.

[43] F. Dai, M. D. Wei, N. W. Xu, Y. Ma, and D. S. Yang. Numerical Assessment of the Progressive Rock Fracture Mechanism of Cracked Chevron Notched Brazilian Disc Specimens. *Rock Mechanics and Rock Engineering*, 48(2):463–479, 2014. ISSN 07232632. doi: 10.1007/s00603-014-0587-8.

[44] M. D. Wei, F. Dai, N. W. Xu, Y. Xu, and K. Xia. Three-dimensional numerical evaluation of the progressive fracture mechanism of cracked chevron notched semi-circular bend rock specimens. *Engineering Fracture Mechanics*, 134:286–303, 2015. ISSN 00137944. doi: 10.1016/j.engfracmech.2014.11.012.

[45] Ramin Ghelichi and Ken Kamrin. Modeling growth paths of interacting crack pairs in elastic media. *Soft Matter*, 11:7995–8012, 2015. ISSN 1744-683X. doi: 10.1039/C5SM01376C. URL `http://pubs.rsc.org/en/content/articlehtml/2015/sm/c5sm01376c`.

[46] Robert Zimmerman and Ian Main. Hydromechanical Behavior of Fractured Rocks. In Yves Gueguen and Maurice Bouteca, editors, *Mechanics of Fluid-Saturated Rocks*, pages 363–421. Elsevier, 2004. ISBN 0074-6142. doi: 10.1016/S0074-6142(03)80023-2.

[47] Adriana Paluszny and Robert W Zimmerman. Numerical simulation of multiple 3D fracture propagation using arbitrary meshes. *Computer Methods in Applied Mechanics and Engineering*, 200(9):953–966, 2011. doi: 10.1016/j.cma.2010.11.013.

[48] Adriana Paluszny and Robert W Zimmerman. Numerical fracture growth modeling using smooth surface geometric deformation. *Engineering Fracture Mechanics*, 108:19–36, 2013. doi: 10.1016/j.engfracmech.2013.04.012.

[49] Morteza Nejati, Adriana Paluszny, and Robert W. Zimmerman. A disk-shaped domain integral method for the computation of stress intensity factors using tetrahedral meshes. *International Journal of Solids and Structures*, 69-70:230–251, 2015. ISSN 00207683. doi: 10.1016/j.ijsolstr.2015.05.026.

[50] Morteza Nejati, Adriana Paluszny, and Robert W. Zimmerman. A finite element framework for modeling internal frictional contact in three-dimensional fractured media using unstructured tetrahedral meshes. *Computer Methods in Applied Mechanics and Engineering*, 306:123–150, 2016. ISSN 00457825. doi: 10.1016/j.cma.2016.03.028.

[51] Ansys, Inc. *ANSYS ICEM CFN User Manual (version 14.5)*, 2012.

[52] Robert D. Cook, David S. Malkus, Michael E. Plesha, and Robert J. Witt. *Concepts and applications of finite element analysis*. John Wiley & Sons, 2007.

[53] N. Barton, S. Bandis, and K. Bakhtar. Strength, deformation and conductivity coupling of rock joints. *International Journal of Rock Mechanics and Mining Sciences*, 22(3):121–140, 1985. ISSN 01489062. doi: 10.1016/0148-9062(85)93227-9.

[54] M. Nejati. *Finite element modelling of frictional contact and stress intensity factors in three-dimensional fractured media using unstructured tetrahedral meshes*. PhD thesis, Imperial College, London, 2015.

[55] T Nakamura and DM Parks. Three-dimensional stress field near the crack front of a thin elastic plate. *ASME, Transactions, Journal of Applied Mechanics*, 55:805–813, 1988. doi: 10.1115/1.3173725.

[56] Morteza Nejati, Adriana Paluszny, and Robert W. Zimmerman. On the use of quarter-point tetrahedral finite elements in linear elastic fracture mechanics. *Engineering Fracture Mechanics*, 144:194–221, 2015. ISSN 00137944. doi: 10.1016/j.engfracmech.2015.06.055.

[57] P. Gupta, C. A. Duarte, and A. Dhankhar. Accuracy and robustness of stress intensity factor extraction methods for the generalized/eXtended Finite Element Method. *Engineering Fracture Mechanics*, 179:120–153, 2017. ISSN 00137944. doi: 10.1016/j.engfracmech.2017.03.035.

[58] H. A. Richard, B. Schramm, and N. H. Schirmeisen. Cracks on mixed mode loading - theories, experiments, simulations. *International Journal of Fatigue*, 62:93–103, 2014. ISSN 01421123. doi: 10.1016/j.ijfatigue.2013.06.019.

[59] H A Richard, M Fulland, and M Sander. Theoretical Crack Path Prediction. *Fatigue and Fracture of Engineering Materials and Structures*, 28:3–12, 2004. doi: j.1460-2695.2004.00855.x.

[60] Soo-ho Chang, Chung-In Lee, and Seokwon Jeon. Measurement of rock fracture toughness under modes I and II and mixed-mode conditions by using disc-type specimens. *Engineering Geology*, 66(1-2):79–97, 2002. doi: 10.1016/S0013-7952(02)00033-9.

[61] M. R.M. Aliha, A. Bahmani, and Sh Akhondi. Determination of mode III fracture toughness for different materials using a new designed test configuration. *Materials and Design*, 86:863–871, 2015. ISSN 18734197. doi: 10.1016/j.matdes.2015.08.033.

[62] M. D. Wei, F. Dai, N. W. Xu, T. Zhao, and K. W. Xia. Experimental and numerical study on the fracture process zone and fracture toughness determination for ISRM-suggested semi-circular bend rock specimen. *Engineering Fracture Mechanics*, 154:43–56, 2016. ISSN 00137944. doi: 10.1016/j.engfracmech.2016.01.002.

[63] T. Cambonie and V. Lazarus. Quantification of the crack fragmentation resulting from mode I+III loading. *Procedia Materials Science*, 3:1816–1821, 2014. ISSN 22118128. doi: 10.1016/j.mspro.2014.06.293.

[64] Jean Baptiste Leblond, Véronique Lazarus, and Alain Karma. Multiscale cohesive zone model for propagation of segmented crack fronts in mode I+III fracture. *International Journal of Fracture*, 191(1-2):167–189, 2015. doi: 10.1007/s10704-015-0001-x.

[65] Barry Kean Atkinson. Subcritical crack growth in geological materials. *Journal of Geophysical Research: Solid Earth*, 89(B6):4077–4114, 1984. doi: 10.1029/JB089iB06p04077.

[66] RJ Charles. Static fatigue of glass. I. *Journal of Applied Physics*, 29(11): 1549–1553, 1958.

[67] Tae Young Ko and John Kemeny. Determination of the subcritical crack growth parameters in rocks using the constant stress-rate test. *International Journal of Rock Mechanics and Mining Sciences*, 59:166–178, 2013. ISSN 13651609. doi: 10.1016/j.ijrmms.2012.11.006.

[68] P. C. Paris and F. Erdogan. A Critical Analysis of Crack Propagation Laws. *Journal of Basic Engineering*, 85(4):528, 1963. ISSN 00219223. doi: 10.1115/1.3656900.

[69] N. Pugno, M. Ciavarella, P. Cornetti, and A. Carpinteri. A generalized Paris' law for fatigue crack growth. *Journal of the Mechanics and Physics of Solids*, 54(7):1333–1349, 2006. ISSN 00225096. doi: 10.1016/j.jmps.2006.01.007.

[70] J M Kemeny. A model for non-linear rock deformation under compression due to sub-critical crack growth. *International Journal of Rock Mechanics and Mining Sciences*, 28(6):459–467, 1991.

[71] Elie Favier, Véronique Lazarus, and Jean Baptiste Leblond. Coplanar propagation paths of 3D cracks in infinite bodies loaded in shear. *International Journal of Solids and Structures*, 43(7-8):2091–2109, 2006. ISSN 00207683. doi: 10.1016/j.ijsolstr.2005.06.041.

[72] M. K. Kassir and G. C. Sih. *Mechanics of Fracture 2, Three-Dimensional Crack Problems*. Noordhoff International Publishing, Leyden, 1975.

[73] Hunjoo P. Lee and Jon E. Olson. The effect of remote and internal crack stresses on mixed-mode brittle fracture propagation of open cracks under compressive loading. *International Journal of Fracture*, 207(2):229–242, 2017. ISSN 0376-9429. doi: 10.1007/s10704-017-0231-1.

[74] L. N. Germanovich, R. L. Salganik, A. V. Dyskin, and K. K. Lee. Mechanisms of brittle fracture of rock with pre-existing cracks in compression. *Pure and Applied Geophysics*, 143(1-3):117–149, 1994. ISSN 00334553. doi: 10.1007/BF00874326.

[75] Arcady V. Dyskin, Leonid N. Germanovich, and Konstantin B. Ustinov.

A 3-D model of wing crack growth and interaction. *Engineering Fracture Mechanics*, 63(1):81–110, 1999. ISSN 00137944. doi: 10.1016/S0013-7944(96)00115-4.

[76] Ping Cao, Taoying Liu, Chengzhi Pu, and Hang Lin. Crack propagation and coalescence of brittle rock-like specimens with pre-existing cracks in compression. *Engineering Geology*, 187:113–121, 2015. ISSN 00137952. doi: 10.1016/j.enggeo.2014.12.010.

[77] S. Nemat-Nasser and H. Horii. Compression-induced nonplanar crack extension with application to splitting, exfoliation, and rockburst. *Journal of Geophysical Research*, 87:6805–6821, 1982. doi: 10.1029/JB087iB08p06805.

[78] W F Brace and E. G. Bombolakis. A note on brittle crack growth in compression. *Journal of Geophysical Research*, 68(12):3709–3713, jun 1963. ISSN 01480227. doi: 10.1029/JZ068i012p03709.

[79] Brian R Lawn. *Fracture of Brittle Solids*. Cambridge University Press, 1993.

[80] E. Hoek and Z. T. Bieniawski. Brittle Fracture Propagation in Rock under Compression. *International Journal of Fracture*, 1(3):137–155, 1965.

[81] H. Horii and S. Nemat-Nasser. Brittle Failure in Compression: Splitting, Faulting and Brittle-Ductile Transition. *Philosophical Transactions of the Royal Society A: Mathematical, Physical and Engineering Sciences*, 319 (1549):337–374, sep 1986. doi: 10.1098/rsta.1986.0101.

[82] M. F. Ashby and C. G. Sammis. The damage mechanics of brittle solids in compression. *Pure and Applied Geophysics PAGEOPH*, 133(3):489–521, 1990. ISSN 00334553. doi: 10.1007/BF00878002.

[83] R N Thomas, A Paluszny, and R W Zimmerman. Effect of fracture growth velocity exponent on fluid flow through geomechanically-grown 3D fracture networks. In *2nd International Discrete Fracture Network Engineering Conference*. American Rock Mechanics Association, 2018.

[84] J. A. Cartwright, C. Mansfield, and B. Trudgill. The growth of normal faults by segment linkage. *Geological Society, London, Special Publications*, 99(1):163–177, 1996. doi: 10.1144/GSL.SP.1996.099.01.13.

[85] W. W. Krech, F. A. Henderson, and K. E. Hjelmstad. A standard rock suite for rapid excavation research. Technical report, U.S. Bureau of Mines, 1974.

[86] Andrew L Thomas and David D. Pollard. The geometry of echelon fractures in rock: implications from laboratory and numerical experiments. *Journal of Structural Geology*, 15(3-5):323–334, 1993. ISSN 01918141. doi: 10.1016/0191-8141(93)90129-X.

[87] V. Cvetkovic, S. Painter, N. Outters, and J. O. Selroos. Stochastic simulation of radionuclide migration in discretely fractured rock near the Äspö Hard Rock Laboratory. *Water Resources Research*, 40(2), 2004. ISSN 00431397. doi: 10.1029/2003WR002655.

[88] Sven Follin, Lee Hartley, Ingvar Rhén, Peter Jackson, Steven Joyce, David Roberts, and Ben Swift. A methodology to constrain the parameters of a hydrogeological discrete fracture network model for sparsely fractured crystalline rock, exemplified by data from the proposed high-level nuclear waste repository site at Forsmark, Sweden. *Hydrogeology Journal*, 22:313–331, 2014. ISSN 1431-2174. doi: 10.1007/s10040-013-1080-2.